nature biomedical engineering

Article

https://doi.org/10.1038/s41551-024-01318-z

A gut-on-a-chip incorporating human faecal samples and peristalsis predicts responses to immune checkpoint inhibitors for melanoma

Received: 9 August 2023

Accepted: 18 November 2024

Published online: 12 February 2025

Check for updates

Mattia Ballerini[1,2], Serena Galiè[1], Punit Tyagi[1], Carlotta Catozzi[1], Hariam Raji[3], Amir Nabinejad[1], Angeli D. G. Macandog[1], Alessandro Cordiale[2], Bianca Ionela Slivinschi[3], Karol K. Kugiejko[1,2], Martina Freisa[1], Paola Occhetta[2], Jennifer A. Wargo[4], Pier F. Ferrucci[5], Emilia Cocorocchio[1,6], Nicola Segata[1,7], Andrea Vignati[1], Andrey Morgun[8], Michela Deleidi[3], Teresa Manzo[9], Marco Rasponi[2] & Luigi Nezi[1]

Patient responses to immune checkpoint inhibitors can be influenced by the gastrointestinal microbiome. Mouse models can be used to study microbiome–host crosstalk, yet their utility is constrained by substantial anatomical, functional, immunological and microbial differences between mice and humans. Here we show that a gut-on-a-chip system mimicking the architecture and functionality of the human intestine by including faecal microbiome and peristaltic-like movements recapitulates microbiome–host interactions and predicts responses to immune checkpoint inhibitors in patients with melanoma. The system is composed of a vascular channel seeded with human microvascular endothelial cells and an intestinal channel with intestinal organoids derived from human induced pluripotent stem cells, with the two channels separated by a collagen matrix. By incorporating faecal samples from patients with melanoma into the intestinal channel and by performing multiomic analyses, we uncovered epithelium-specific biomarkers and microbial factors that correlate with clinical outcomes in patients with melanoma and that the microbiome of non-responders has a reduced ability to buffer cellular stress and self-renew. The gut-on-a-chip model may help identify prognostic biomarkers and therapeutic targets.

Since their introduction in the clinic, immune checkpoint inhibitors (ICIs) have achieved unprecedented and durable results in the treatment of cancers, especially in the case of melanoma[1–6]. ICIs act on inhibitory signalling pathways that have evolved to restrain uncontrolled inflammatory responses that, in pathologic conditions, are exploited by the tumour to evade immune surveillance[7,8]. The prototypes of ICIs are monoclonal blocking antibodies directed against surface receptors expressed on T cells (such as programmed cell death protein 1, PD-1; and cytotoxic T-lymphocyte-associated protein, CTLA-4) or on antigen presenting cells and tumours (such as programmed death-ligand 1, PD-L1) that enhance antitumour immunity. After over a decade, patient responses to ICIs remain heterogeneous[9], and questions persist about optimal combinations and toxicities[10,11].

In addition to tumour-intrinsic mechanisms, the gut microbiome has emerged as a major tumour-extrinsic factor able to predict and drive immunotherapy outcomes[12–15]. The gut microbiome includes the genes and metabolic functions of bacteria, archaea, viruses, fungi and protists in the intestine[16–18]. It is spatially and functionally restrained

A full list of affiliations appears at the end of the paper. e-mail: luigi.nezi@ieo.it

by the intestinal mucosa, which acts as a physical barrier against pathogens while contributing to the beneficial homeostatic interplay between microbiota and the immune system[19]. Perturbation of the gut homeostasis can impair epithelial cell–cell adhesions, favour pathogens' translocation and lead to a state of chronic inflammation[19–22] that may influence antitumour immunity and responses to therapy, especially ICI treatment[23]. Yet, there is no clinical indication for prescribing an intestinal biopsy during immunotherapy, which limits the investigation of molecular mechanisms underlying microbiome–host crosstalk in situ and the possibility to discriminate the role played by the intestinal epithelial cells from other components of the microenvironment.

In this regard, mouse models are broadly used as preclinical experimental systems, but their value in translational research is limited by anatomical, functional, immunological and microbial differences with humans[24–27], in addition to their high cost, experimental time and ethical concerns. As an alternative, the three-dimensional (3D) culture of primary human intestinal organoids[28] offers greater cellular heterogeneity and architectural complexity compared with conventional two-dimensional (2D) cell culture, but they cannot be easily exposed to controlled peristaltic-like motions, microorganisms or drugs. Indeed, due to their inverted structural arrangement, the apical compartment is enclosed within the lumen and has an altered environment and limited access[25,29,30]. Microfluidic-based approaches overcome most of these limitations, and their miniaturization reduces quantities of samples and reagents and enables detection at high resolution and sensitivity, with scalable throughput and shorter data processing and analysis[31–33].

In this Article, we present a system that mimics the architecture and functionality of the human intestine and that is suitable for studying microbiome–host interactions. It relies on intestinal cells co-cultured with microvascular endothelial cells on a compartmentalized microfluidic 3D system actuated with a peristaltic-like motion. We employ it to dissect the effects, in their intestine, of the microbiota of patients with melanoma who are responsive or non-responsive to immunotherapy, and provide mechanistic insights.

Results

Development of the gut-on-a-chip

Human gut-on-a-chip models currently address one or a few aspects of the intestinal epithelial physiology, either enabling co-culturing multiple cell types, using extracellular matrix (ECM) for compartmentalization, applying shear forces and mechanical stretch, or providing ready access to the luminal spaces for experimental perturbations[25,34,35]. Leveraging on proprietary actuation technology[36,37], we developed a gut-on-a-chip model that integrates them all-in-one and is suitable for real-time multiomic detections. The model consists of an intestinal channel and a vascular compartment separated by an ECM-like gel layer (Fig. 1a,b; see Methods for details). While the intestinal channel is seeded with either human induced pluripotent stem cell (hiPSC)-derived organoids or a co-culture of Caco-2 and HT-29 MTX, the vascular compartment is formed by human microvascular endothelial cells (HMEC-1), which retain the morphologic, phenotypic and functional characteristics of the normal human microvascular endothelium while offering the advantages of an immortalized cell line[38].

Mechanical actuation shapes intestinal epithelium

The use of hiPSC-derived intestinal organoids (Fig. 1c) on a chip would potentially enable tailored studies on any healthy participant or patient, with the advantage of allowing access to both the apical and the basal epithelial compartments[39–42]. Thus, we adapted previous methods to seed our device with hiPSC-derived intestinal organoids (Methods and Extended Data Fig. 1a), obtaining a proliferating (Ki67) and polarized (apical localization of villin and of the zonula occludens-1 protein, ZO-1) intestinal barrier (Fig. 1d–f) populated with different physiologically relevant intestinal cell types, including epithelial cells (E-cadherin or E-cad), goblet cells (mucin 2, MUC2 and mucin 5AC, MUC5AC), enteroendocrine cells (chromogranin A) and Paneth cells (lysozyme) (Fig. 1g).

Next, we investigated the impact of peristaltic-like movements on the hiPSC-derived intestine-on-chip. We observed that mechanical stimulation (deformation 10–15%; frequency 0.2 Hz; 9 days of culturing, 7 days of actuation; Extended Data Fig. 1b) increased proliferation (Ki67, static percentage = 5.44 ± 1.18 versus actuated percentage = 16.44 ± 8.14) especially at collagen matrix border (Extended Data Fig. 1c), polarization (villin expression static percentage = 90.80 ± 13.08 versus actuated percentage = 150.20 ± 10.45) and mucus production (MUC5AC, $Area_{static}$ = 8,977 ± 7,303 μm^2, $Area_{actuated}$ = 42,382 ± 11,921 μm^2; MUC2, $Area_{static}$ = 1,141 ± 549 μm^2, $Area_{actuated}$ = 8,205 ± 280 μm^2; Fig. 1h,i). All this was accompanied by an enhanced formation of 3D supra-cellular villi-like structures (Fig. 1j,k), in agreement with previous reports[42].

Similar results were obtained when the intestinal epithelial tubule was generated by co-culturing Caco-2 (enterocyte-like absorptive and brush-forming)[43] and HT-29MTX (mucin-secreting)[44] human colorectal carcinoma cell lines. Indeed, despite containing only two intestinal cell types, such simplified model is functionally mature, fully polarized and responsive to mechanical strain (Ki67, static percentage = 9.23 ± 4.30 versus actuated percentage = 16.94 ± 6.33; villin expression static percentage = 18.26 ± 9.19 versus actuated percentage = 74.54 ± 14.30; MUC5AC, $Area_{static}$ = 21,509 ± 10,656 μm^2, $Area_{actuated}$ = 138,616 ± 23,449 μm^2), as shown by the expression of functional, proliferative and lineage markers (Fig. 2a,b). In particular, the overt increase in mucin production (Fig. 2c), which was restricted to MUC5AC in this system (compare Fig. 2b and Extended Data Fig. 2a,b), and 3D villi-like structures (Fig. 2d,e) are crucial for conducting microbiome–host studies.

As endothelial cells are known to modulate growth and function of intestinal epithelial cells[38], next we seeded Caco-2 and HT-29MTX cells in one of the two channels of the chip and cultured them in the presence or absence of HMEC-1 in the other (Fig. 2f and Extended Data Fig. 2c). The expression of villin ($MFI_{normal\ medium}$ = 29.21 ± 7.87, $MFI_{medium\ endo}$ = 27.53 ± 9.20, $MFI_{co\text{-}culture}$ = 46.69 ± 6.22) and ZO-1 ($MFI_{normal\ medium}$ = 35.02 ± 5.23, $MFI_{medium\ endo}$ = 34.00 ± 3.18, $MFI_{co\text{-}culture}$ = 46.87 ± 9.38) increased in epithelial cells upon co-culturing with HMEC-1 cells, indicative of a tighter and more mature intestinal barrier (Extended Data Fig. 2e). Accordingly, permeability to dextran decreased as early as after 5 days of culture ($P_{app\ normal\ medium}$ = 1.88 × 10^{-5} ± 1.58 × 10^{-6} cm s^{-1}, $P_{app\ medium\ endo}$ = 1.42 × 10^{-5} ± 2.38 × 10^{-6} cm s^{-1}, $P_{app\ co\text{-}culture}$ = 2.29 × 10^{-7} ± 1.14 × 10^{-7} cm s^{-1}; Extended Data Fig. 2e–g), confirming that co-culturing with microvascular endothelial cells speeds the maturation of the intestinal epithelium into a functional and selective barrier and making the system suitable to dissect complex molecular interactions engaging both compartments. In addition, evaluation of the barrier functionality using different fluorescent dextrans confirmed that the two tubular structures are independent, with a measured permeability of 1.01 × 10^{-7} ± 2.14 × 10^{-8} cm s^{-1} at epithelial side (tetramethylrhodamine isothiocyanate (TRITC)-dextran, red) and 1.41 × 10^{-7} ± 7.69 × 10^{-9} cm s^{-1} at microvascular side (fluorescein isothiocyanate (FITC)-dextran, green, Fig. 2g and Extended Data Fig. 2h,i).

Transcriptional changes in the gut-on-a-chip mimic epithelial responses

Intestinal microbes impact about 10% of the host's transcriptome, primarily including genes involved in immunity, cell proliferation and cell metabolism[45]. To define the response of the model to the microbiota, we compared transcriptional profiles of our gut-on-a-chip generated from Caco-2 and HT-29MTX cells upon exposure to whole faecal samples from patients with melanoma (Live) or their abiotic supernatants (Sup). Principal component analysis (PCA) highlighted how the microbiota influenced the intestinal epithelium (Fig. 3a), with more pronounced changes in samples treated with faeces (turquoise, 3,278 differentially

https://doi.org/10.1038/s41551-024-01318-z

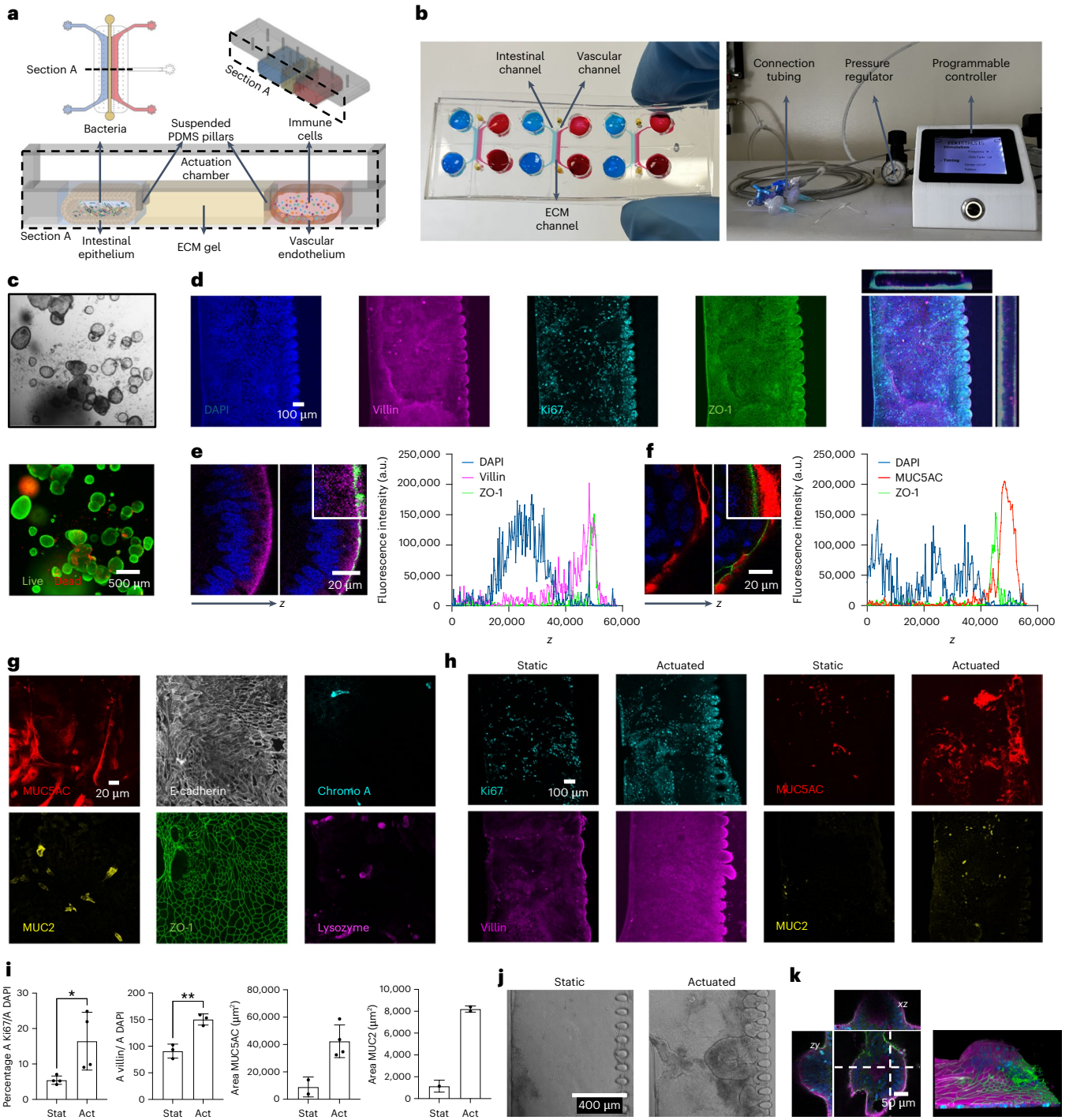

Fig. 1 | The hiPSCs-derived gut-on-a-chip model. a, The device is composed of an intestinal epithelial channel and a vascular endothelial channel separated by ECM-like gel; a superimposed actuation chamber allows cyclic controlled deformation of the construct that mimics peristalsis. PDMS, polydimethylsiloxane. **b**, Microfluidic device and external actuation system. **c**, Brightfield and live/dead fluorescence image of hiPSCs-derived organoids in plate. **d**, Representative confocal images ($n = 13$ in 2 independent experiments) of intestinal cells from disaggregated hiPSCs-derived organoids after 9 days of culture on chip. DAPI (blue), ZO-1 (green), Ki67 (cyan) and villin (magenta). **e**,**f**, Epithelial cells polarization from disaggregated organoids. Representative confocal image and fluorescence intensity plot on *z* axis of nuclei (DAPI, blue) and apical occludins (ZO-1, green) in combination either with villin (magenta, **e**) or MUC5AC (red, **f**). **g**, Representative confocal images ($n > 4$ in 2 independent experiments) of the different intestinal cell lineages from disaggregated hiPSCs-derived organoids after 9 days of culture on chip. MUC5AC (red), MUC2 (yellow), E-cadherin (white), ZO-1 (green), chromogranin A (cyan, Chromo A) and lysozyme (magenta). Chromo A, chromogranin A. **h**,**i**, Fluorescence microscopy images (**h**) and quantification (**i**) of Ki67 (cyan), villin (magenta), MUC5AC (red) and MUC2 (yellow) in static versus actuated chips. Mechanical actuation resulted in increased proliferation (Ki67, $n_{static} = 4$, $n_{actuated} = 4$, $P = 0.0368$), maturation (villin, $n_{static} = 3$, $n_{actuated} = 3$, $P = 0.0035$) and mucus production (MUC5AC, $n_{static} = 2$, $n_{actuated} = 4$; MUC2, $n_{static} = 1$, $n_{actuated} = 2$). Bars represent mean ± s.d., two-tailed unpaired *t*-test. $^{*}P \leq 0.05$; $^{**}P \leq 0.01$. A, area; Stat, static chips; Act, actuated chips. **j**, Representative brightfield images ($n > 8$ in 2 independent experiments) of epithelial cells from disaggregated hiPSCs-derived organoids cultured in static versus actuated conditions highlighting the formation of 3D villi-like structures. **k**, Representative confocal images ($n = 13$ in 2 independent experiments) and 3D reconstruction of villi-like structure on chip. Dashed lines indicate the axis along with the (*x*,*z*) and (*z*,*y*) confocal images used for the reconstructions where taken.

https://doi.org/10.1038/s41551-024-01318-z

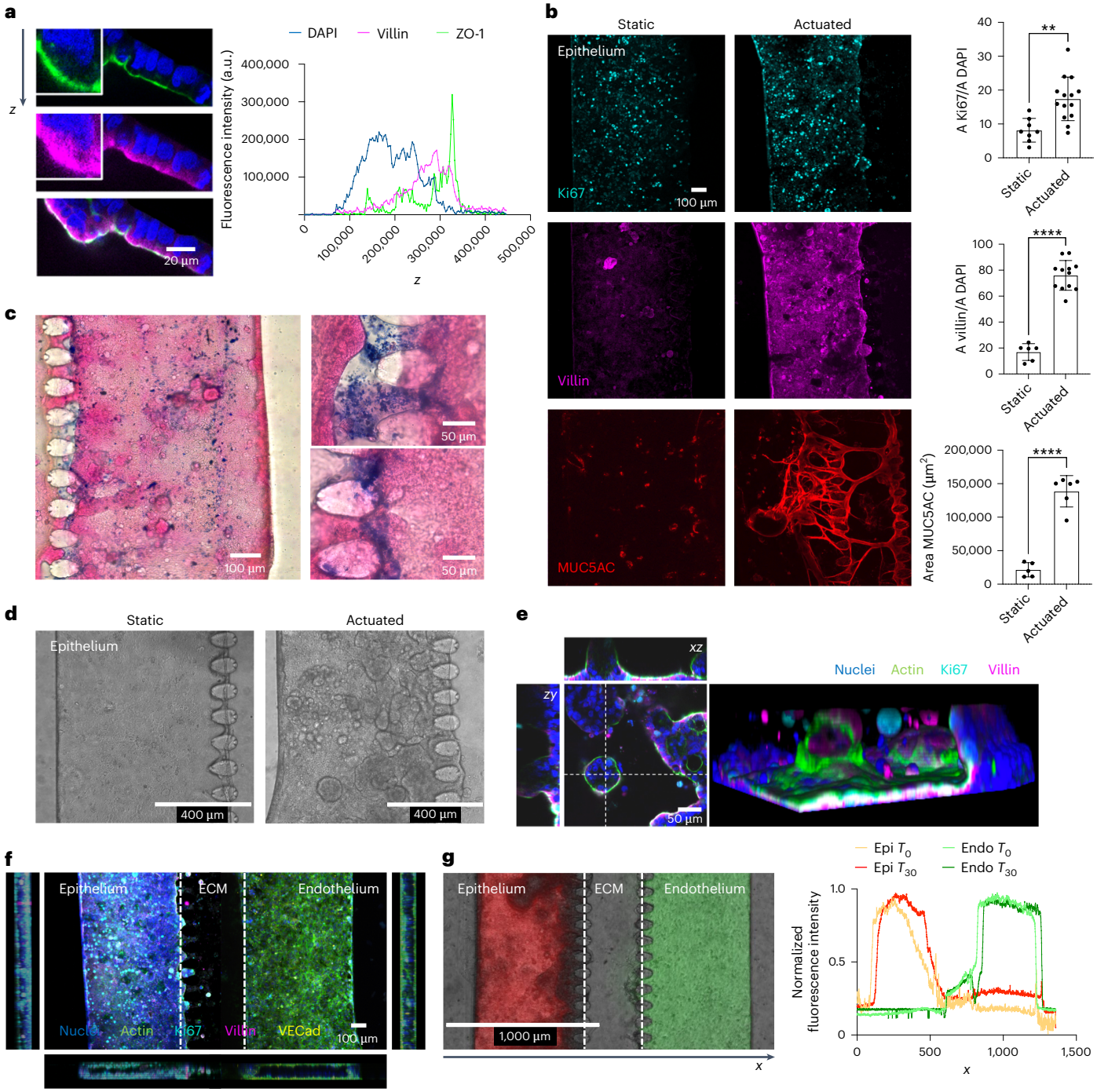

Fig. 2 | The gut-on-a-chip model. a, Epithelial cells polarization. Representative confocal image and fluorescence intensity plot on *z* axis of nuclei (DAPI, blue), apical occludins (ZO-1, green) and villin (magenta). **b**, Fluorescence microscopy images and quantification of Ki67 (cyan), villin (magenta) and MUC5AC (red) in static versus actuated chips. Mechanical actuation resulted in increased proliferation (Ki67, $n_{static} = 8$, $n_{actuated} = 14$, $P = 0.0013$), maturation (villin, $n_{static} = 6$, $n_{actuated} = 12$, $P = 3.3 \times 10^{-9}$) and mucus production (MUC5AC, $n_{static} = 5$, $n_{actuated} = 6$, $P = 2.91 \times 10^{-6}$). Bars represent mean ± s.d., two-tailed unpaired *t*-test. $^{**}P \leq 0.01$; $^{****}P \leq 0.0001$. A, area. **c**, Representative histological images ($n = 4$ in 2 independent experiments) of epithelial cells stained with eosin (magenta) for cells and Alcian blue (blue) for the secreted mucus layer. **d**, Brightfield images of epithelial cells cultured in static versus actuated conditions highlighting the formation of 3D villi-like structures. **e**, Representative confocal images and 3D reconstruction of villi-like structure on chip. Dashed lines indicate the axis along with the (*x*,*z*) and (*z*,*y*) confocal images used for the reconstructions where taken. **f**, Representative confocal images ($n > 100$ chambers in >30 independent experiments) of epithelial (Caco-2 and HT-29 MTX) and endothelial (HMEC-1) cells after 9 days of culture. DAPI (blue), phalloidin (green), Ki67 (cyan), villin (magenta) and VE-cadherin (VECad; yellow). **g**, Functional permeability assay. Fluorescence microscopy image ($T = 30$ min) and intensity profile (T_0 = injection of dextran, $T_{30} = 30$ min) of TRITC-dextran 4.4 kDa (red) and FITC-dextran 40 kDa (green) on epithelial and endothelial barriers, respectively, at day 9. Data were normalized on maximum value. Epi, epithelial; Endo, endothelial.

expressed genes (DEGs), 2,960 unique, $P < 0.01$) compared with faecal supernatants (orange, 1,119 DEGs, 801 unique, $P < 0.01$; Extended Data Fig. 3a) despite extensive overlapping at the level of upregulated and downregulated functions (Fig. 3b). Gene set enrichment analysis (GSEA) highlighted a major reprogramming of the epithelium treated with faeces and, to a lesser extent, with supernatants, which was characterized by activation of pathways of response to pathogens, tumour necrosis factor (TNF), nuclear factor kappa-light-chain-enhancer of activated B cells (NF-κB), neutrophil-to-lymphocyte ratio and cytokine signalling, and downregulation of genes involved in cell cycle and mitochondrial metabolism (Fig. 3c,d and Extended Data Fig. 3b), in line with previous reports[46]. Among those modulated by both treatments (yellow, 318 DEGs $P < 0.01$; Extended Data Fig. 3a), a subgroup of genes was downregulated only by faeces (163 DEGs, $P < 0.01$; Extended Data Fig. 3c), which impacted interleukin-17 (IL-17) and TNF signalling, cell cycle and apoptosis, among others (Extended Data Fig. 3d).

As experimental manipulation of microbiota in mice is still the most accessible approach to dissect microbiome–host interactions in vivo, next we compared the transcriptome of the gut-on-a-chip model upon exposure to faeces with publicly available datasets of microdissected villous epithelial cells from conventional (specific pathogen-free, $n = 6$) or germ-free ($n = 6$) mice[46] (Fig. 3e). First, the 3,278 significant DEGs ($P < 0.01$) were obtained after treating the in vitro system with faeces, and then the enriched gene ontology (GO) terms were mapped to those 786 GSEA-enriched GO terms obtained in the comparison of specific pathogen-free with germ-free mice. Second, among the 786 GSEA's enriched terms shared between the gut-on-a-chip and mouse intestinal villi, we found a subset of pathways similarly modulated in both systems (Fig. 3g). The resulting analysis identified a fraction of human–mouse orthologous GO terms concordantly regulated by the microbiome in vitro and in vivo (X^2 test = 0.0001; Fig. 3f). In particular, the intestinal epithelium exposed to the microbiome upregulated inflammatory, pattern recognition receptors (PRRs), metabolic and death receptor signalling, paired with a downregulation of mitochondrial and cell cycle functions, in vitro as well as in vivo (Fig. 3g; Methods). Thus, this gut-on-a-chip model is suitable to study the host–microbiome crosstalk, and, even in its simplest version, it enables biologically relevant observations that could complement (and potentially reduce) the use of animal models.

The gut-on-a-chip reveals pro-inflammatory traits in non-responsive patients

Response to ICI treatment is, to a certain extent, modulated by the gut microbiome[12–14,47]. Still, we are far from reliably predicting how the melanoma of individual patients will respond to immunotherapy solely based on the analysis of their gut microbiome[23,48]. In this regard, heterogeneous outcomes of therapeutic faecal microbiota transplantation in combination with ICI[49–51] indicated a still limited knowledge of basic mechanisms involved in the gut microbiome–host crosstalk and their clinical impact. Therefore, we used the gut-on-a-chip model to evaluate specific effects on the intestinal epithelium of the gut microbiome of patients with melanoma responsive or non-responsive to immunotherapy (Fig. 4a). PCA analysis of transcriptomes of mature intestinal epithelial barriers on-chips exposed to fresh-frozen faecal material from patients with melanoma that were responsive or non-responsive (Fig. 4b) revealed that chips treated with faeces from non-responsive patients acquired distinct profiles compared with controls ($n = 6$, $P < 0.05$), while effects of faeces from responsive patients were more heterogeneous and limited to a smaller number of DEGs ($n = 4$; Fig. 4b,c). Still, faeces from both groups of patients induced a generalized suppression of cell cycle, DNA replication and repair machineries, of mitochondrial biogenesis and transport, chromatin organization, autophagy and protein metabolism, which were noticeable in non-responsive patients (especially regarding the cell cycle, DNA replication and repair, protein metabolism) and less in responsive patients (limited to chromatin organization; Extended Data Figs. 4a–c). These downregulations were coupled with upregulation of interleukin and death receptor signalling (that is, TNF-related apoptosis-inducing ligand; Fig. 4d and Extended Data Fig. 5a–c), matching what has been previously observed in vivo[52–56]. However, only faeces from non-responsive patients elicited major transcriptional reprogramming, suppressing pathways of cellular response to stress (both chemical and hypoxic), RNA metabolism and transcription, signal transductions (that is, NOTCH, Hedgehog, WNT, MAPK4/5), non-canonical NF-κB and IL-12 signalling and apoptosis, while inducing TNF and IL-6, vascular endothelial growth factor (VEGF), RET[57] and Rho GTPases signalling (Extended Data Figs. 4a–c and Fig. 3d). Overall, our gut-on-a-chip model revealed that faeces from non-responsive patients have substantial pro-inflammatory effects on the intestinal epithelium, which may negatively impact the response of these patients to immunotherapy[23].

Gut-on-a-chip response to microbiota matches immunotherapy data

Based on the emerged pro-inflammatory capability of faecal samples from non-responsive patients, next we used quantitative confocal microscopy on intact gut-on-a-chip models to compare them with those from responsive patients, measuring markers of acute toxicity (that is, caspase-3), barrier integrity (that is, ZO-1) and cellular signalling (that is, β-catenin). While the caspase-3 staining increased independently from the source of the faecal microbiome ($MFI_{CTR} = 7.51 \pm 3.35$, $MFI_{NR} = 13.33 \pm 3.27$, $MFI_{R} = 13.91 \pm 3.94$), we observed a brisk reduction of ZO-1 ($MFI_{CTR} = 41.25 \pm 6.69$, $MFI_{NR} = 20.83 \pm 5.37$, $MFI_{R} = 38.35 \pm 3.72$) and β-catenin expression ($MFI_{CTR} = 44.59 \pm 5.58$, $MFI_{NR} = 13.80 \pm 4.94$, $MFI_{R} = 50.40 \pm 8.75$) only when treating with faeces from patients with melanoma who were non-responsive (Fig. 5a,b), while gut microbiota from responsive patients resembled those of healthy donors (HD, $n = 3$) and did not impact the integrity of the intestinal barrier, in terms of adherens or of tight junctions (E-cad: $MFI_{CTR} = 53.43 \pm 8.89$, $MFI_{NR} = 25.61 \pm 2.37$, $MFI_{R} = 89.31 \pm 34.34$, $MFI_{HD} = 65.90 \pm 7.10$; ZO-1: $MFI_{CTR} = 45.48 \pm 4.26$, $MFI_{NR} = 19.52 \pm 2.47$, $MFI_{R} = 44.88 \pm 2.64$, $MFI_{HD} = 45.96 \pm 1.36$; Extended Data Fig. 6a,b). The fact that similar changes were observed when operating in anaerobic conditions (Extended Data Figs. 6c,d) excludes—within our limits of detection—that they may result from technical artefacts and supports their biological relevance.

The effects of gut microbiota from non-responsive patients on the intestinal epithelium were coupled with loss of the microvascular barrier integrity (vascular endothelial cadherin (VE-cadherin), $MFI_{CTR} = 16.84 \pm 0.74$, $MFI_{NR} = 12.44 \pm 2.08$, $MFI_{R} = 23.58 \pm 3.63$) and activation of the microvascular endothelial cells, as measured by the expression of the Intercellular Adhesion Molecule 1 (ICAM-1, $MFI_{CTR} = 0.53 \pm 0.09$, $MFI_{NR} = 15.73 \pm 6.20$, $MFI_{R} = 4.43 \pm 3.11$; Fig. 5c,d), suggesting that, differently from those from responsive patients, faeces from non-responsive patients challenge the homeostatic state of intestinal tissues.

Importantly, faeces from both patient's groups had comparable bacterial load (as measured by non-selective culturing in aerobic as well as in anaerobic conditions; Extended Data Fig. 6e,f) and, together with whole-genome metagenomic sequencing analysis, supported that divergent effects caused by faeces of patients with melanoma that were responsive versus those that were non-responsive are likely due to qualitative (relative abundance) rather than quantitative (overall amount of living bacteria) differences (Fig. 6a), in accordance with previous reports[12–14]. However, lack of consensus on microbes linking the immune modulation with ICI outcome still precludes unambiguous classification of commensal species as 'good' or 'bad'[48]. By contrast, functional redundancies across cohorts support the concept that bacterial function may be at least as relevant as phylogeny for the host–microbiome dialogue. As resistance of patients to immunotherapy has

https://doi.org/10.1038/s41551-024-01318-z

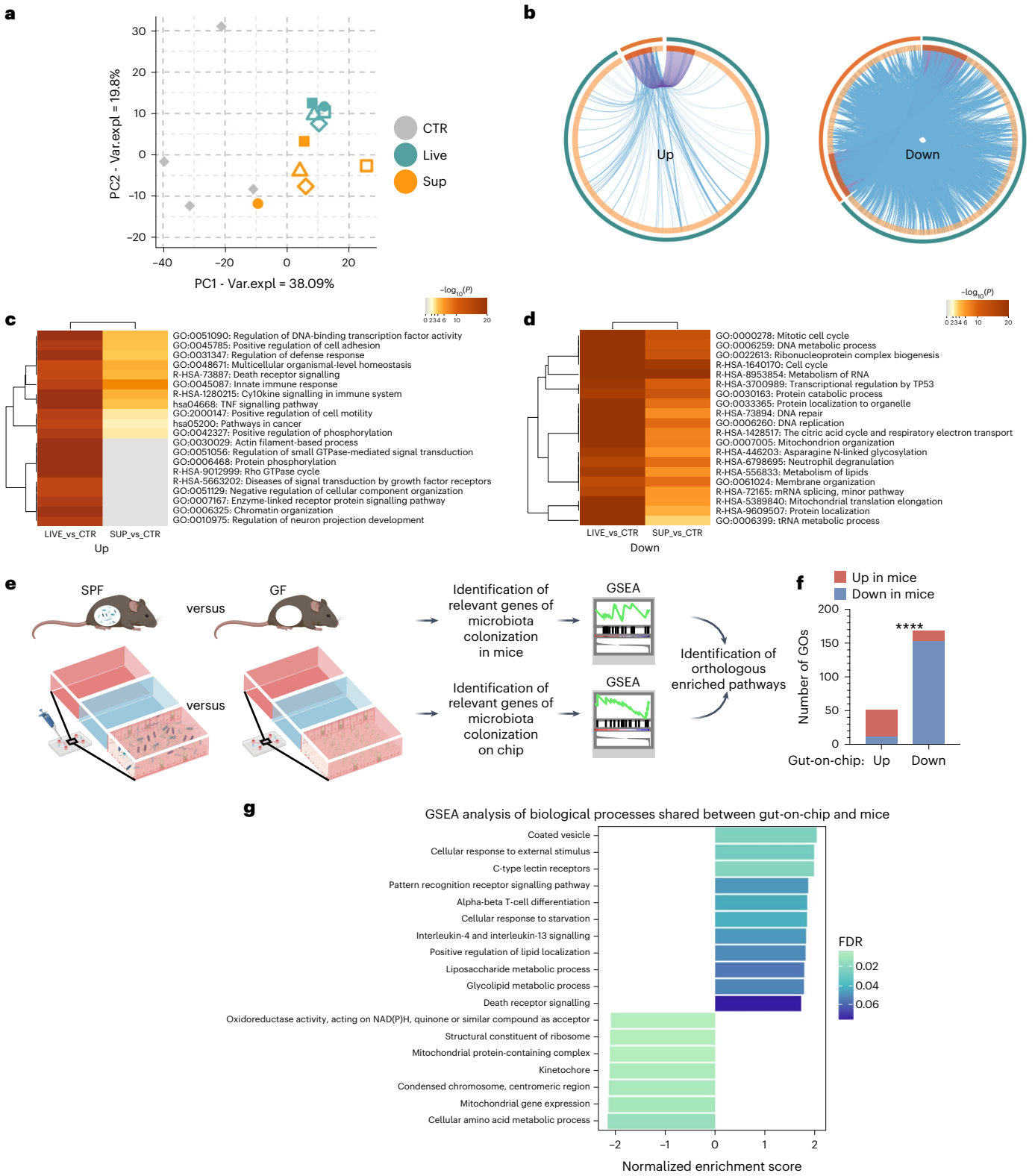

Fig. 3 | The gut-on-a-chip recapitulates biologically relevant aspects of the in vivo response to faecal microbiota. a, PCA plot of untreated (CTR) and treated gut-on-a-chip with whole faeces (Live) or faecal supernatant (Sup). Var.expl, variance explained. **b**, Overlap between upregulated (left) or downregulated (right) DEGs in Live versus CTR (turquoise, outer circle) or Sup versus CTR (orange, outer circle), only at the gene level (with purple lines linking identical genes) or including the shared term level (with blue lines linking genes that belong to the same enriched ontology term). The inner circle represents common (dark orange) or unique (light orange) DEG in the two lists. **c**,**d**, Heat map of enriched terms (top 20 clusters) across upregulated (**c**) or downregulated (**d**) DEGs in Live versus CTR (left columns) or Sup versus CTR (right columns), coloured by *P* values. **e**, Experimental workflow. The transcriptomes of control chips and epithelial cells treated with live bacteria were compared with transcriptomes of germ-free (GF) mice and specific pathogen-free (SPF) mice. **f**, Number (*y* axis) of shared upregulated and downregulated GO terms between the gut-on-a-chip (*x* axis) and mice (coloured bars). Chi-square test indicates GOs concordantly regulated in the two systems. ****$P < 0.0001$. **g**, Bar plot of enriched biological processes in the gut-on-a-chip and mice upon exposure to faecal microbiome. Normalized enrichment score coloured by false discovery rate values.

https://doi.org/10.1038/s41551-024-01318-z

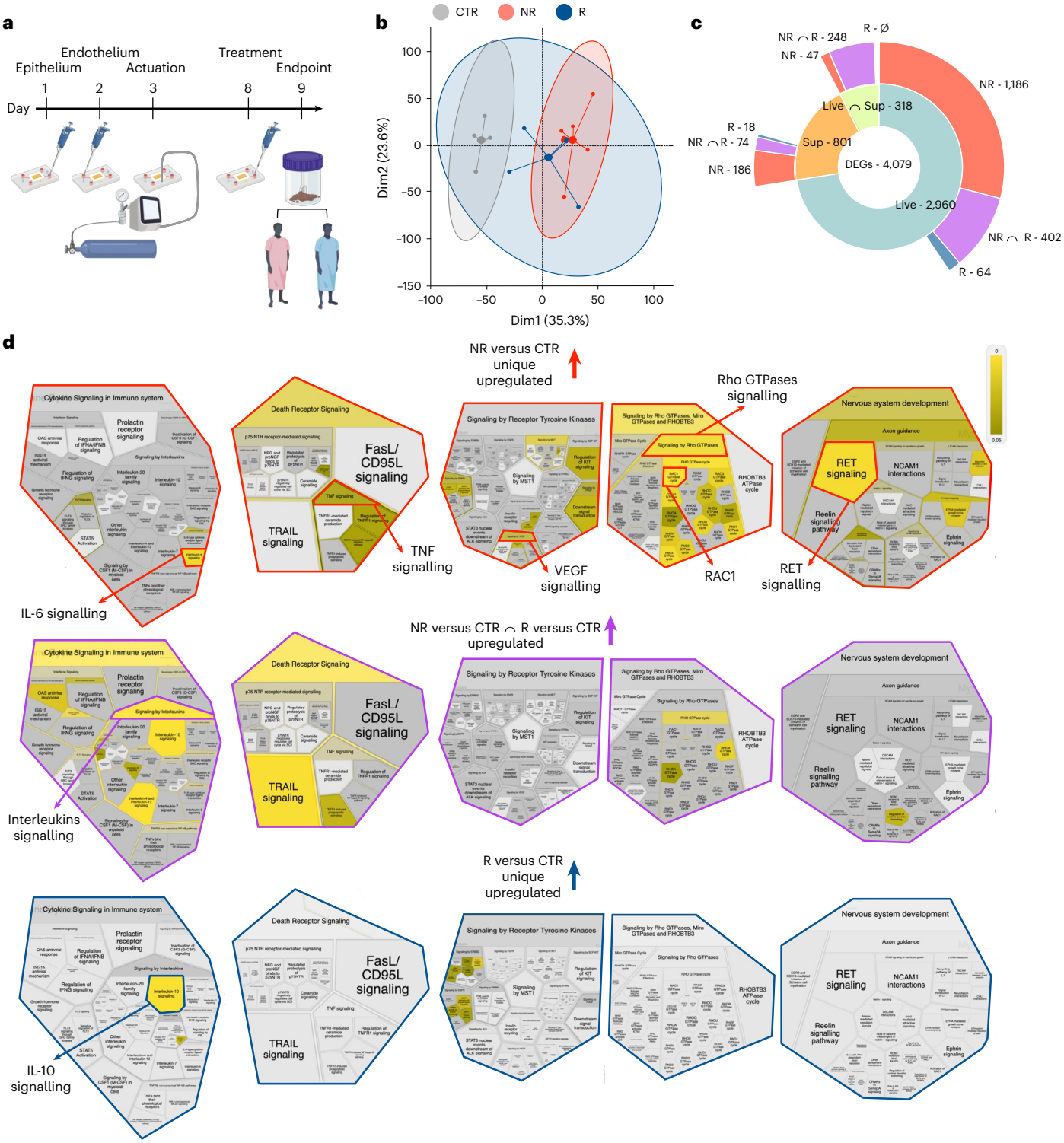

Fig. 4 | Transcriptional profiling of the gut-on-a-chip response to faecal microbiota from patients with melanoma undergoing immunotherapy. **a**, Experimental design. Complete gut-on-a-chip were treated (day 8) with faecal material from patients with melanoma responsive (R, blue) or non-responsive (NR, red) to immunotherapy. **b**, PCA plot of untreated (CTR) and treated gut-on-a-chip with faecal material from responsive (R) patients and non-responsive (NR) patients. Dim1, dimension 1; Dim2, dimension 2. **c**, Sunburst plot showing the indicated number of DEGs, unique or shared (purple and light lime), in the gut-on-a-chip treated with whole faeces (Live, turquoise) or faecal supernatants (Sup, orange) from patients with melanoma that were responsive (blue) or non-responsive (red) compared with untreated controls (CTR). **d**, Reactome's pathway analysis of NR versus CTR (red) and R versus CTR (blue) unique and common (purple) DEGs coloured by normalized enrichment score.

https://doi.org/10.1038/s41551-024-01318-z

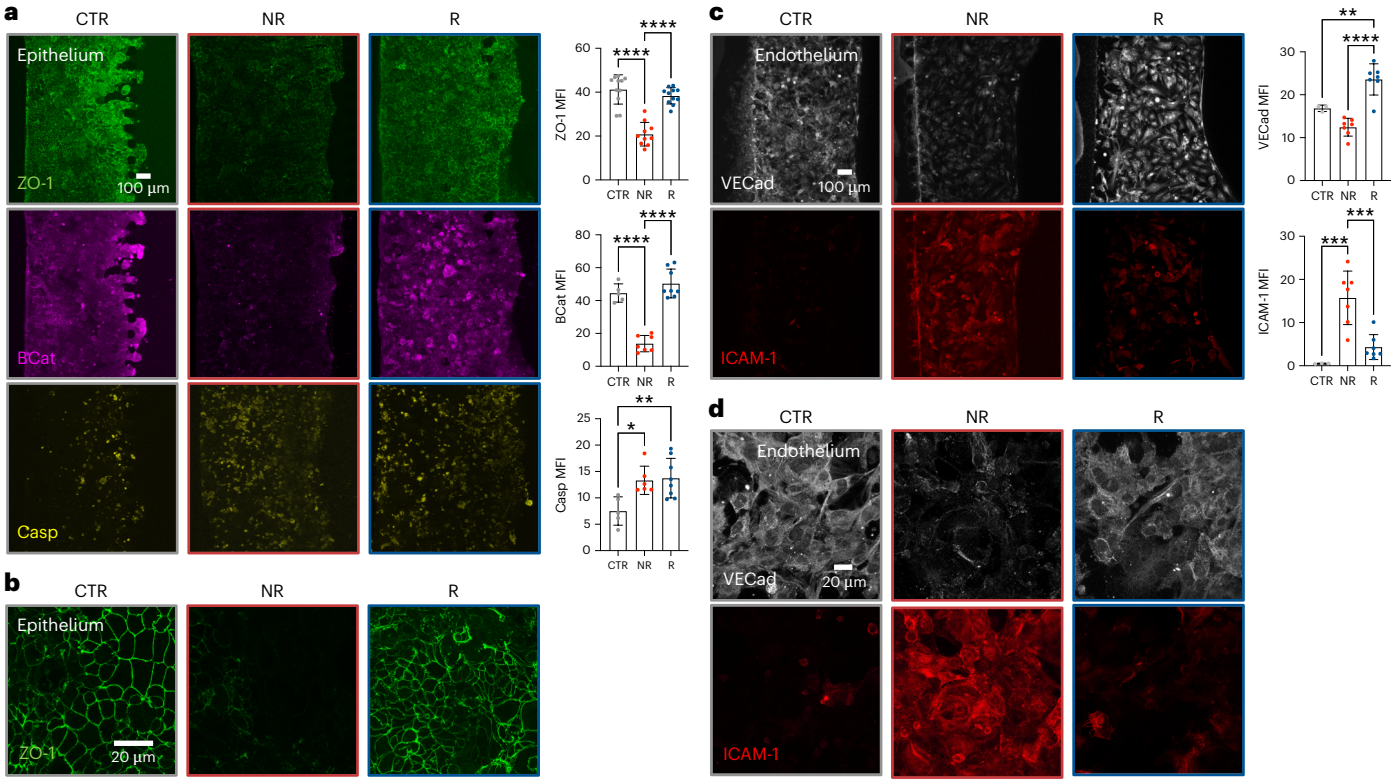

Fig. 5 | The gut-on-a-chip distinguishes faecal microbiota of non-responsive patients from faecal microbiota of responsive patients. a, Representative fluorescence microscopy images and mean fluorescence intensity (MFI) quantification of ZO-1 (green, at least 3 independent replicates per patient, $P = 4.7 \times 10^{-9}$ for CTR versus NR and $P = 1.03 \times 10^{-7}$ for R versus NR), β-catenin (BCat, magenta, at least 2 independent replicates per patient, $P = 1.97 \times 10^{-6}$ for CTR versus NR and $P = 3.04 \times 10^{-8}$ for R versus NR) and caspase-3 (Casp, yellow, at least 2 independent replicates per patient, $P = 0.0215$ for NR versus CTR, $P = 0.0093$ for R versus CTR) on untreated gut-on-a-chip (CTR) or after 24 h treatment with faeces (10 mg ml^{-1}) from patients with melanoma R or NR to immunotherapy. Bars represent mean ± s.d., ordinary one-way analysis of variance (ANOVA). **b**, Representative high-magnification fluorescence microscopy images ($n > 15$ in 6 independent experiments) of ZO-1 on untreated gut-on-a-chip (CTR) or after 24 h treatment with faeces (10 mg ml^{-1}) from patients with melanoma R or NR to immunotherapy. **c**, Representative fluorescence microscopy images and MFI quantification of VE-cadherin (VECad, white, at least 2 independent replicates per patient, $P = 0.0084$ for R versus CTR, $P = 7.38 \times 10^{-6}$ for R versus NR) and ICAM-1 (red, at least 2 independent replicates per patient, $P = 0.0006$ for R versus CTR, $P = 0.0008$ for R versus NR) on endothelial cells in control chips (CTR) or after 24 h treatment with faeces as in **a**. Bars represent mean ± s.d., ordinary one-way ANOVA. *$P \leq 0.05$; **$P \leq 0.01$; ***$P \leq 0.001$; ****$P \leq 0.0001$. **d**, Representative high-magnification fluorescence microscopy images ($n = 7$ in 3 independent experiments) of VE-cadherin (white) and ICAM-1 (red) on endothelial cells in control chips (CTR) or after 24 h treatment with faeces as in **a**.

been previously associated with lipopolysaccharides (LPS) produced by Gram-negative bacteria[23,58], we searched for LPS-related bacterial genes in the faecal metagenomes of our patients with melanoma, confirming that they were enriched in the faeces of non-responsive patients compared with those that were responsive (Fig. 6b and Extended Data Fig. 6g). This finding well matched the transcriptional changes observed upon treatment with faeces from non-responsive patients, with activation of LPS/Toll-like receptor (TLR)'s downstream signalling (that is IL-6, TNF, Rho GTPases)[59].

Therefore, we exposed the gut-on-a-chip model to LPS from *Escherichia coli* and recorded effects on the epithelial barrier. Similar to faeces of non-responsive patients, we observed a loss of barrier function upon LPS treatment ($P_{app\_CTR} = 8.82 \times 10^{-8} \pm 1.08 \times 10^{-9}$ cm s^{-1} versus $P_{app\_LPS} = 1.17 \times 10^{-5} \pm 4.13 \times 10^{-6}$ cm s^{-1}; Fig. 6c–e) coupled with a downregulation of ZO-1 ($MFI_{CTR} = 38.11 \pm 8.27$, $MFI_{LPS} = 23.17 \pm 5.16$) and E-cadherin ($MFI_{CTR} = 53.60 \pm 3.13$, $MFI_{LPS} = 26.01 \pm 4.09$) expression on epithelial cells (Fig. 6f,h and Extended Data Fig. 7a,b). It is worth noting that our gut-on-a-chip model showed a range of responses that reflected structural and immunostimulatory differences of the LPS produced by different bacteria[60–62], suggesting that microbiota from non-responsive patients may be particularly enriched in LPS resembling the hexa-acylated LPS from *E. coli* or the monophosphorylated, penta-acylated LPS from *Porphyromonas gingivalis* (Extended Data Fig. 7a,b).

Nevertheless, we also recorded an increase in ICAM-1 on HMEC-1 cells upon LPS treatment ($MFI_{CTR} = 1.16 \pm 0.68$, $MFI_{LPS} = 14.86 \pm 12.73$; Fig. 6g,h), and, when we injected isolated human T cells in the preformed microvascular channel, they adhered more (CTR = 45.40 ± 16.80, LPS = 77.14 ± 10.41; Fig. 6i), likely as a consequence of HMEC-1 activation. In conclusion, using the gut-on-a-chip model, we demonstrated that faeces from non-responsive patients have a higher pro-inflammatory effect compared with faeces from responsive patients, and that this is due, at least in part, to a higher activation of LPS-dependent signalling.

Soluble factors from the microbiota of non-responsive patients mimic LPS inflammatory effects

The therapeutic potential of faecal microbiota transplantation in combination with ICI has been demonstrated in preclinical and clinical settings[12–14,49–51]. However, which components of the faecal microbiome are sufficient to elicit favourable or detrimental effects in the gut is contentious, and safety[63] related to the use of live bacteria is still a major concern. We sought to determine whether soluble factors produced by faecal communities from responsive patients and non-responsive patients were sufficient to recapitulate the effects of stools. When exposed to faecal supernatants from either responsive patients or non-responsive patients, the gut-on-a-chip model showed that soluble faecal factors from non-responsive patients were sufficient

https://doi.org/10.1038/s41551-024-01318-z

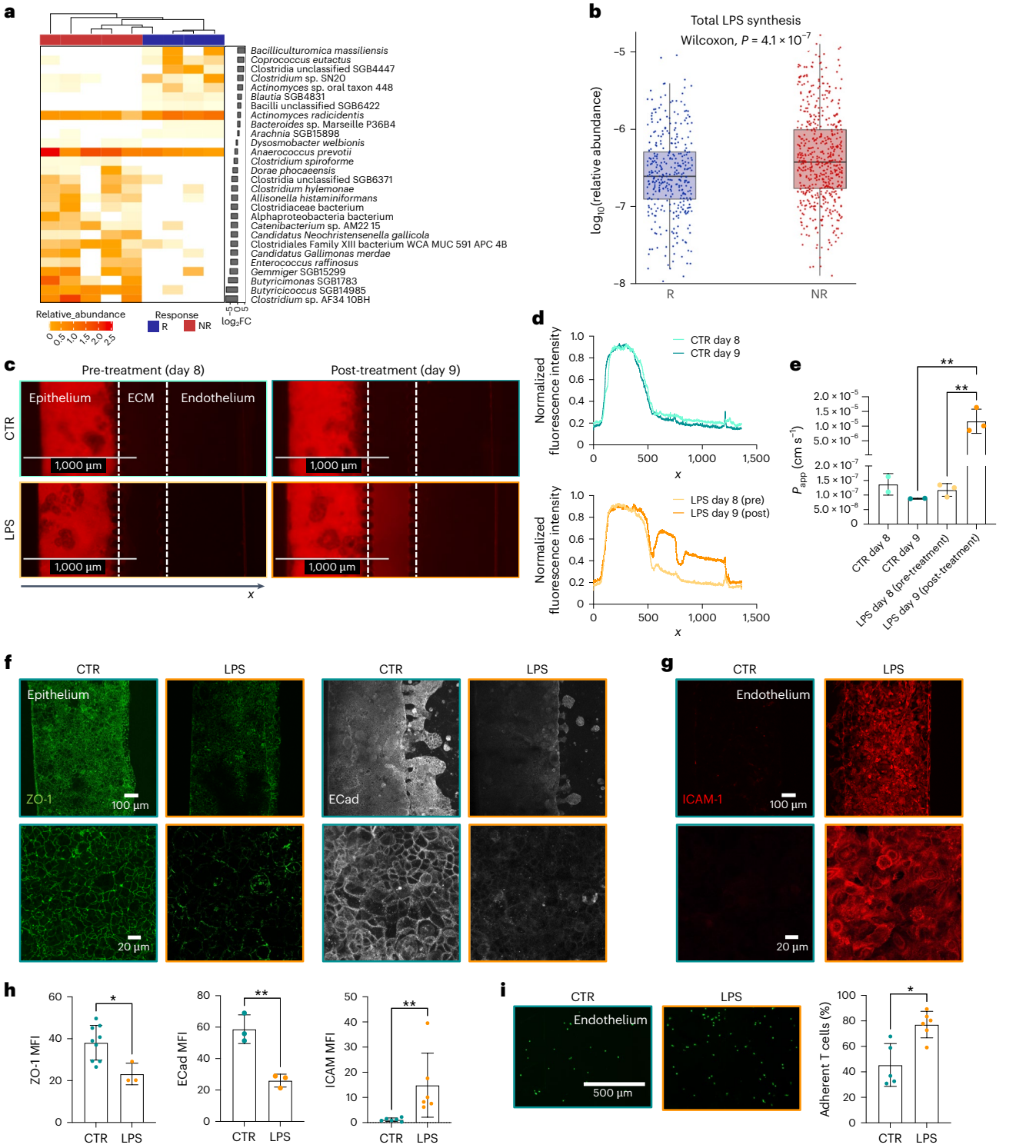

Fig. 6 | Treatment with LPS produces similar effects as faecal microbiota from non-responsive patients on the gut-on-a-chip. a, Heat map of top R- and NR-associated taxa based on Wilcoxon test unadjusted $P < 0.05$. Bars on the right indicate $\log_2$ fold change of mean relative abundance (R/NR). **b**, Relative abundances (in a $\log_{10}$ base) of detected UniRef90 genes involved in LPS synthesis in patients' faeces ($n_{NR} = 5$, $n_R = 4$, two-tailed Wilcoxon rank-sum test $P = 4.1 \times 10^{-7}$). **c**, Fluorescence microscopy images ($n > 2$ in 2 independent experiments) of dextran permeability assay (TRITC-dextran 4.4 kDa) on epithelial cells at day 8 (left) and day 9 (right) in control chips (top) and LPS-treated (24 h, 10 µg ml^{-1}) chips (bottom). **d**, Normalized fluorescence intensity profile of dextran permeability assay (TRITC-dextran 4.4 kDa) of control and LPS-treated chips at day 8 and day 9. Data were normalized on maximum value. **e**, Apparent permeability (P_{app}) quantification of epithelial barrier in control and LPS-treated chips at day 8 and day 9 ($P = 0.0072$ for LPS day 9 versus CTR day 9, $P = 0.0041$ for LPS day 9 versus LPS day 8). **f**, Fluorescence microscopy images of ZO-1 (green) and E-cadherin (ECad, white) on epithelial cells in control and LPS-treated chips. **g**, Fluorescence microscopy images of ICAM-1 (red) on endothelial cells in control chips and after LPS treatment of epithelial tubule. **h**, Mean fluorescence intensity quantification of ZO-1 ($P = 0.0182$), E-cadherin (ECad, $P = 0.0041$) and ICAM-1 ($P = 0.0022$). **i**, Fluorescence microscopy images and quantification of adherent T cells (green, $P = 0.0157$) on endothelial cells cultured in endothelial medium or pre-treated with LPS. Bars represent mean ± s.d., ordinary one-way ANOVA (**e**), two-tailed Mann–Whitney test (**h** left and right), two-tailed unpaired t-test (**h** centre), two-tailed paired t-test (**i**) and Wilcoxon test (**b**). *$P \leq 0.05$; **$P \leq 0.01$.

https://doi.org/10.1038/s41551-024-01318-z

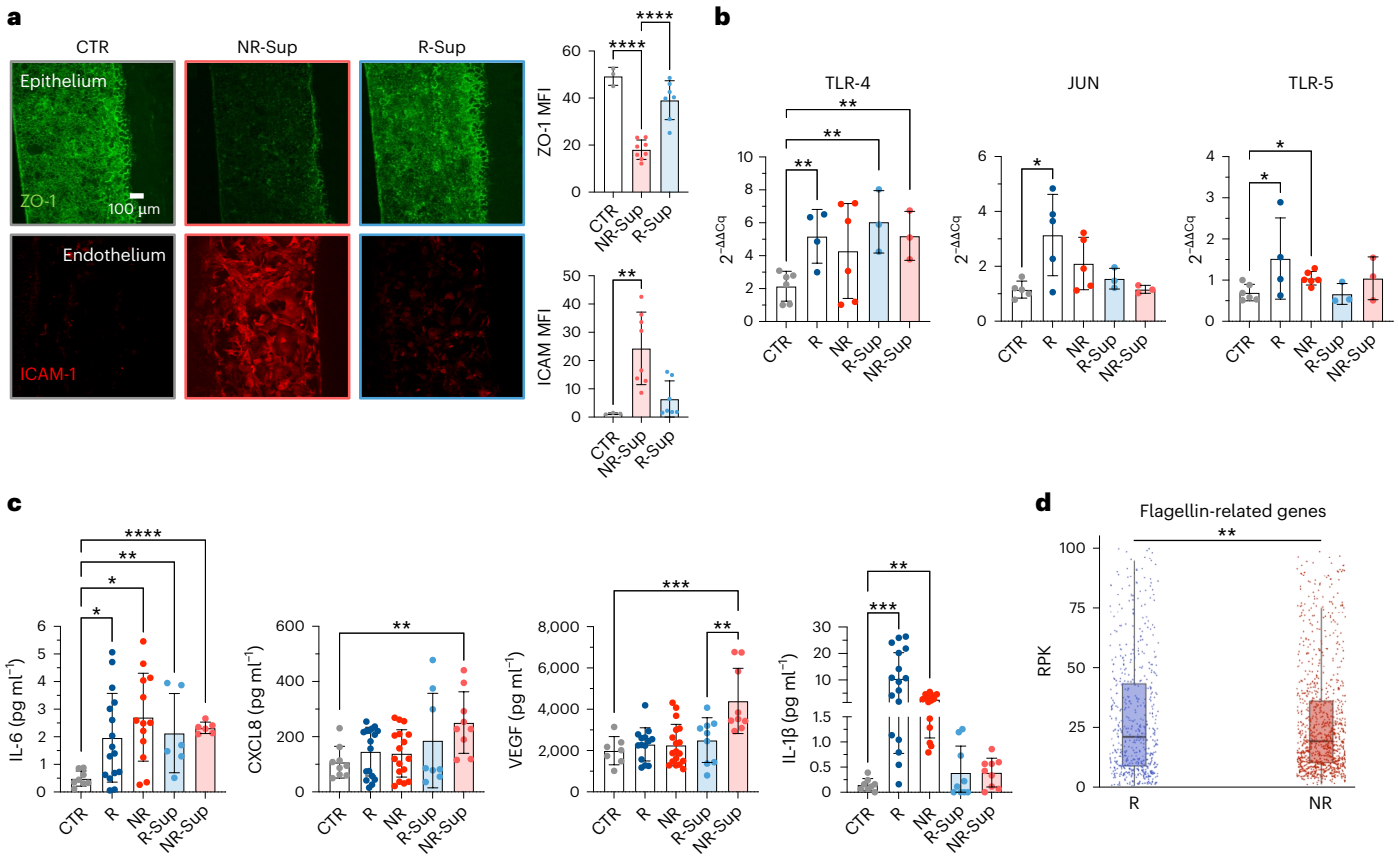

Fig. 7 | Faecal microbiota from responsive patients and non-responsive patients elicit different inflammatory responses on-chip. a, Fluorescence microscopy images and quantification of ZO-1 (green, $P = 4.99 \times 10^{-6}$ for CTR versus NR and $P = 2.19 \times 10^{-5}$ for R versus NR) and ICAM-1 (red, $P = 0.0034$) in control chips (CTR) or after treatment with faecal supernatant from R or NR patients. At least 2 independent replicates per patient. **b**, TLR-4, JUN and TLR-5 expression (qPCR analysis) in CTR or epithelial cells treated with faeces or faecal supernatants from R or NR (TLR-4, $P = 0.0051$ for R versus CTR, $P = 0.0034$ for R-Sup versus CTR, $P = 0.0058$ for NR-Sup versus CTR; JUN, $P = 0.0226$; TLR-5, $P = 0.0333$ for R versus CTR, $P = 0.0152$ for NR versus CTR). At least 1 independent replicate per patient. **c**, Multiplex ELISA (Luminex) quantification of IL-6 ($P = 0.0181$ for R versus CTR, $P = 0.001$ for NR versus CTR, $P = 0.0075$ for R-Sup versus CTR, $P = 1.07 \times 10^{-8}$ for NR-Sup versus CTR), CXCL8 ($P = 0.0019$), VEGF ($P = 0.0007$ for NR-Sup versus CTR, $P = 0.0078$ for NR-Sup versus R-Sup) and IL-1β ($P \leq 0.01$ for NR-Sup versus CTR, $P \leq 0.001$ for NR-Sup versus R-Sup) released by CTR or epithelial cells treated with complete faecal material or faecal supernatants of R and NR patients. At least 2 independent replicates per patient. **d**, Normalized abundance (RPK) of bacterial flagellin-related gene terms in R and NR metagenomes ($P = 0.00841$). Whiskers equal to 1.5 times inter-quartile range, two-tailed Wilcoxon rank-sum test. Bars represent mean ± s.d., ordinary one-way ANOVA (**a** top and **c**), Kruskal–Wallis test (**a** bottom). $^{*}P \leq 0.05$; $^{**}P \leq 0.01$; $^{***}P \leq 0.001$; $^{****}P \leq 0.0001$. RPK, reads per kilobase.

to induce a decrease in ZO-1 in epithelial cells ($MFI_{CTR} = 49.27 \pm 3.82$, $MFI_{NR} = 18.06 \pm 4.13$, $MFI_{R} = 39.08 \pm 8.28$), which was coupled with an increase in ICAM-1 on micro-endothelial cells ($MFI_{CTR} = 1.22 \pm 0.29$, $MFI_{NR} = 24.33 \pm 12.83$, $MFI_{R} = 6.41 \pm 6.41$). Conversely, treatment with faecal supernatants from responsive patients did not have a major impact on barrier integrity compared with controls (Fig. 7a,b). These data were corroborated by the induction of TLR-4 expression (the LPS receptor) upon treatment with either whole faeces or supernatants (Fig. 7c). Moreover, we measured in the effluent media of the gut-on-a-chip higher levels of inflammatory molecules known to be released in response to LPS, such as IL-6, CXCL8[59,64], CCL20[65] and VEGF[66,67], and this was more evident upon treatment with supernatants from non-responsive patients (Fig. 7d). Interestingly, when inflammatory molecules where quantified in parallel in the microvascular channel, the effect of supernatants non-responsive patients was even more pronounced compared with the treatments with faecal samples, especially in the case of interferon-γ (IFNγ) (Extended Data Fig. 8a,b).

Although we noticed a generalized increase in the release of IL-1β following the exposure to different microbial components, it was particularly higher in the presence of whole faeces from responsive patients, both in aerobic and anaerobic conditions (Fig. 7d and Extended Data Fig. 8c, respectively), mirroring the expression of its transcriptional regulator JUN[68] (Fig. 7b, which confirmed results of the upstream analysis presented in Extended Data Fig. 5b). This was a specific trait of the microbiota of responsive patients, which otherwise induced a pattern of response such as the one from healthy donors (Extended Data Fig. 8d). Observations linking high-levels of the IL-1β to the integrity of the intestinal barrier[69–71] are often conflicting, likely because of overlapping mechanisms engaged by damage and homeostatic repair of the intestine. As previous work conducted on mouse models showed that TLR-5 activation cooperates with IL-1β and IL-10 signalling in resolving intestinal inflammation[72–74], we analysed how TLR-5 expression changed on the gut-on-a-chip upon microbiome exposure—having already shown that treatment with faeces from responsive patients specifically increased IL-10 signalling (Fig. 4d). In agreement with a coordinated regulation of these three signalling in response to a peculiar composition of the microbiota, we found that TLR-5 expression increased following treatment with whole faeces, especially with those from responsive patients (Fig. 7b). The involvement of TLR-5 signalling in the response to faeces from responsive patients was further supported by gene-level metagenomic analysis of faecal samples, which revealed a higher abundance of flagellin-related genes in responsive patients than in non-responsive patients (Fig. 7d)—with flagellins being the natural ligand of TLR-5.

Testing therapeutic potential of microbiota factors on-chip

Finally, aiming to develop targeted strategies to improve ICI efficacy based on gut microbiota manipulations, the therapeutic potential of faecal samples from patients with melanoma responding to immunotherapy was evaluated on the gut-on-a-chip model. We observed that combining whole faecal material or supernatants from responsive patients was able to ameliorate the effects of faeces from non-responsive patients on the intestinal barrier integrity, as measured by ZO-1, E-cad and BCat expression on epithelial cells (ZO-1: $MFI_{CTR} = 49.87 \pm 5.92$, $MFI_{NRSup} = 31.69 \pm 3.69$, $MFI_{NRSup+RSup} = 49.63 \pm 4.14$, $MFI_{NRSup+R} = 48.62 \pm 4.91$; E-cad: $MFI_{CTR} = 49.48 \pm 9.27$, $MFI_{NRSup} = 29.56 \pm 2.08$, $MFI_{NRSup+RSup} = 55.09 \pm 5.69$, $MFI_{NRSup+R} = 66.69 \pm 4.36$; BCat: $FI_{CTR} = 43.41 \pm 4.92$, $MFI_{NRSup} = 25.19 \pm 2.89$, $MFI_{NRSup+RSup} = 36.63 \pm 5.00$, $MFI_{NRSup+R} = 54.22 \pm 3.22$; Fig. 8a,b). Similarly, both whole faecal material and supernatants from responsive patients were able to counteract LPS-induced disruption of the intestinal epithelial barrier (ZO-1: $MFI_{LPS} = 23.17 \pm 5.16$, $MFI_{LPS+RSup} = 58.54 \pm 8.75$, $MFI_{LPS+R} = 60.63 \pm 4.38$; E-cad $MFI_{LPS} = 26.01 \pm 4.09$, $MFI_{LPS+RSup} = 62.89 \pm 13.18$, $MFI_{LPS+R} = 69.52 \pm 2.94$; BCat: $MFI_{LPS} = 27.51 \pm 2.18$, $MFI_{LPS+RSup} = 68.51 \pm 5.21$, $MFI_{LPS+R} = 57.67 \pm 10.28$; Fig. 6a,d). These results were corroborated by the reduction of VEGF, CXCL-8 and IL-6 released in the epithelial channel when supernatant from responsive patients was added to the treatment with supernatant from non-responsive patients (Fig. 8e), supporting an overall beneficial effect of responsive patients microbiota-derived products on the inflammatory state of the intestinal barrier.

Combined treatment with purified flagellin (*Salmonella typhimurium*) achieved similar benefits, in terms of both barrier integrity and control of inflammatory factors (Fig. 8c–e), while it was not able to rescue the disruptive effect of the exposure to purified LPS (Fig. 8c,d).

In summary, our findings show that the response of melanoma to immunotherapy can be predicted based on effects elicited by patient-derived faecal samples on our gut-on-a-chip, which is also suitable for dissecting mechanistic details underlying the interactions of different components of the microbiota with host and to foster their development into new therapeutics.

Discussion

We have developed a microfluidic-based gut-on-a-chip model that overcomes some of the limitations of current 2D, 3D and in vivo systems and that provides a reliable system to study microbiome–host interactions. Functional tubular structures such as this gut-on-a-chip have previously been reported in other models[29,30,75,76]. However, the use of an ECM-like gel instead of an artificial porous polydimethylsiloxane membrane[29,30] at interface between the epithelial and the micro-vascular channels provides this system with a more physiological solution framed in a highly functional design, which allows cell or particle tracking between compartments directly on an intact chip. In addition, replacing an alternate flow[75,76] with a superimposed actuation chamber enables controlled stimulation of the device, introducing peristaltic-like mechanical forces that modulate cellular signalling involved in the development and the homeostasis of the epithelium while generating a dynamic luminal environment.

Despite these implementations and the presence of different intestinal cell types derived from the use of hiPSC, the model does not reproduce the physiology of the human intestine in its whole. While here we define the limits within which the system can generate biologically relevant responses, studies are underway to address some outstanding points, including microfluidic-based solutions for long-term anaerobic culture, adjusting the complexity and physiological composition of the ECM, introducing a resident immune compartment and integrating the whole system with a patient-derived melanoma model on-chip. In this regard, we have applied multiomic approaches to accurately quantify molecular mechanisms underlying the response of the intestinal epithelium to faecal microbiome, recapitulating key transcriptional modulations observed in mouse models, for example. Even in its simpler version with Caco-2 and HT29MTX cell lines, the gut-on-a-chip helps tracing individual contributions of epithelial, microvascular and immune components back to the complexity of microbiome–host interactions. This is a crucial step toward its use to complement in vivo experiments and in preclinical studies, especially during the discovery and de-risking stages, which will speed the design of targeted interventions while minimizing the use of experimental animals.

It is worth noting that, going beyond the experimental validation of the system, here we have tested clinically relevant human faecal samples directly on-chip, generating results that confirm preclinical and clinical observations while untangling unappreciated properties of biotic and abiotic components of the faecal microbiota in patients with melanoma. In this regard, we have provided initial evidence of transcripts, soluble molecules and bacterial components associated with specific clinical features. If confirmed in larger cohorts and with independent approaches, they may represent the foundation of objective multivariate biomarkers of response to ICI (that is, based on targeted quantitative PCR (qPCR) and multiplexed enzyme-linked immunosorbent assay (ELISA)) that is even more accessible and time and cost effective.

Based on quantitative measurements correlated with the clinical outcome, we have shown that the faecal microbiome of patients with melanoma that were responsive or non-responsive exert different effects on the gut. In particular, we provide evidence that the microbiome of non-responsive patients, which has been already associated with an altered intestinal epithelial homeostasis[23], is characterized by reduced ability to buffer cellular stress (that is, oxidative stress related to nuclear factor erythroid 2-related factor 2), to renew and to heal, likely leading to a state of persistent inflammation. In addition, our data assigned different clinical relevance to soluble components and microorganisms in faeces, with the former dominated by LPS in

Fig. 8 | Gut-on-a-chip reveals therapeutic potential of faecal microbiota from responsive patients. a,**b**, Fluorescence microscopy images (**a**) and relative quantification (**b**) of ZO-1, E-cadherin and β-catenin on epithelium treated with faecal supernatant from NR patients and LPS combined with faecal material or supernatant from R patients (ZO-1: $P = 0.0161$ for NR-Sup versus CTR, $P < 0.001$ for NR-Sup versus NR-Sup+R, LPS versus CTR, LPS versus LPS+R-Sup, LPS versus LPS+R; ECad: $P = 0.0271$ for NR-Sup versus CTR, $P = 0.0271$ for CTR versus LPS+R, $P < 0.001$ LPS versus CTR, for LPS versus LPS+R, NR-Sup versus NR-Sup+R, NR-Sup versus NR-Sup+R-Sup, LPS versus LPS+R-Sup; BCat: $P = 0.0403$ for CTR versus NR-Sup+R, $P = 0.0054$ for CTR versus LPS+R, $P = 0.0048$ for NR-Sup+R versus NR-Sup+R-Sup, $P < 0.001$ for NR-Sup versus CTR, LPS versus CTR, CTR versus LPS+R-Sup, NR-Sup versus NR-Sup+R, LPS versus LPS+R-Sup, LPS versus LPS+R). **c**,**d**, Fluorescence microscopy images (**c**) and relative quantification (**d**) of ZO-1 and E-cadherin on epithelium treated with faecal supernatant from NR patients and LPS combined with flagellin (ZO-1: $P = 0.0046$ for NR-Sup versus CTR, $P = 0.0020$ for NR-Sup versus flagellin, $P = 0.0017$ for NR-Sup versus NR-Sup+flagellin, $P < 0.0001$ for LPS versus CTR, LPS+flagellin versus CTR, LPS versus flagellin, LPS+flagellin versus flagellin, NR-Sup+flagellin versus LPS+flagellin; ECad: $P = 0.0013$ for NR-Sup versus CTR, $P = 0.0341$ for CTR versus NR-Sup+flagellin, $P = 0.0112$ for flagellin versus NR-Sup, $P = 0.0026$ for flagellin versus LPS+flagellin, $P < 0.001$ for LPS versus CTR, NR-Sup versus NR-Sup+flagellin, NR-Sup+flagellin versus LPS+flagellin, LPS+flagellin versus CTR, flagellin versus LPS). **e**, Multiplexed ELISA (Luminex) of VEGF ($P = 0.0016$ for NR-Sup versus CTR), CXCL8 ($P = 0.0496$ for NR-Sup versus CTR) and IL-6 ($P < 0.001$ for CTR versus R-Sup, NR-Sup versus CTR, NR-Sup versus R-Sup, NR-Sup versus NR-Sup+R-Sup, NR-Sup versus NR-Sup+flagellin) released by controls or epithelium treated with faecal supernatant from NR patients combined with supernatant from R patients or flagellin. Bars represent mean ± s.d., Kruskal–Wallis test (**e** left and centre) ordinary one-way ANOVA (**b**, **d**, **e** right). $^{*}P \leq 0.05$; $^{**}P \leq 0.01$; $^{***}P \leq 0.001$; $^{****}P \leq 0.0001$.

https://doi.org/10.1038/s41551-024-01318-z

non-responsive patients and the latter enriched in flagellin-related genes in responsive patients. Studies on and off the chip are underway to decode the complex heterogeneity of these molecules and their downstream signalling.

One of the main obstacles to continuation of ICI treatments is the appearance of high-grade immune-related adverse events, including severe colitis. While frequently limiting the benefits of the therapy, ICI-associated colitis can be rescued, at least in part, by manipulating

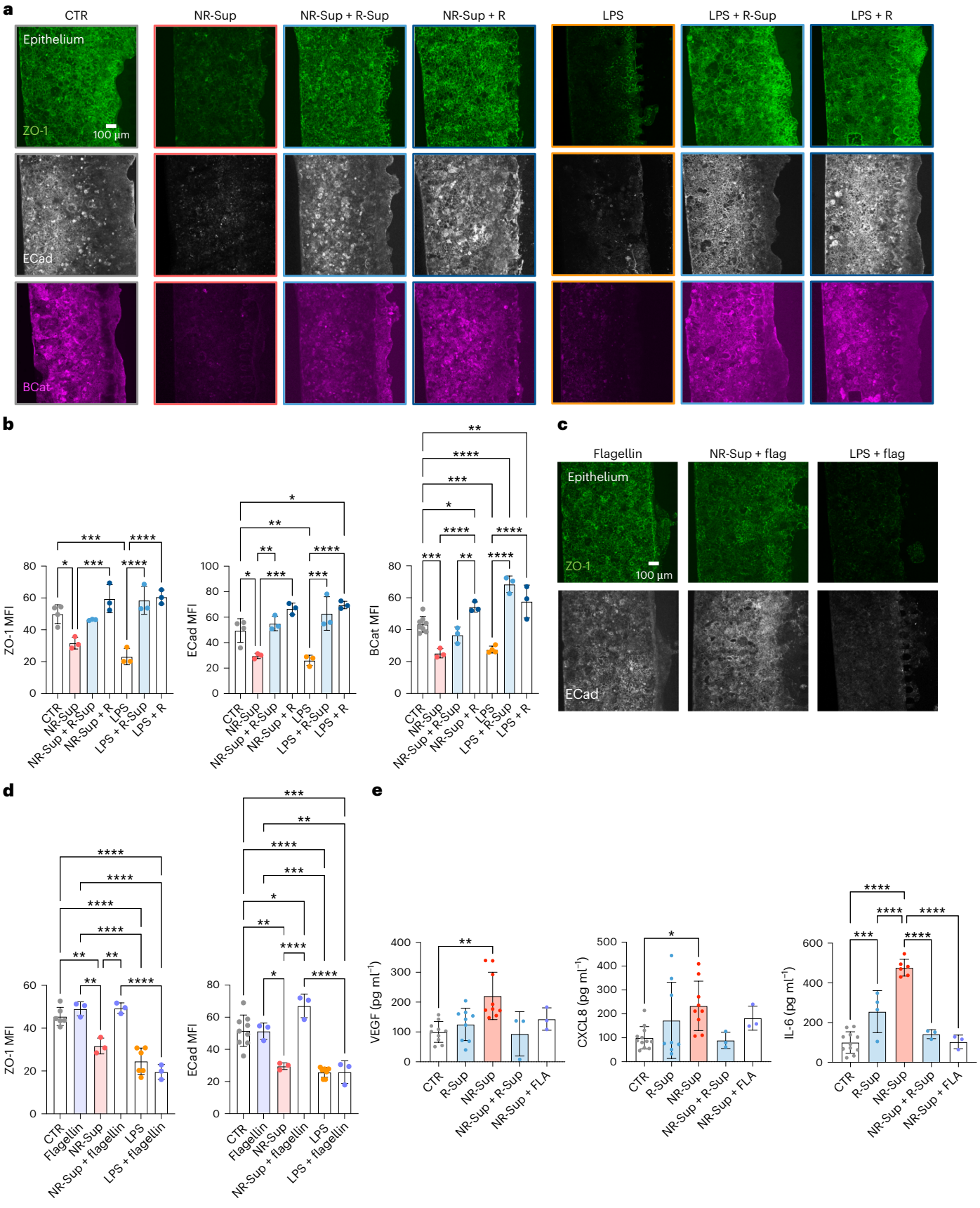

the gut microbiota[77,78]. We have previously demonstrated that immune-related adverse events associate with higher IL-1β levels and peculiar microbial compositions in patients[79], suggesting potential targets for intervention. Protective effects of IL-1β have been reported in the skin, where bacteria-induced IL-1β release resulted in skin regeneration after injury[80], and in the gut, where IL-1β promoted T_{reg} functions and induced immunoglobulin A production[81,82]. Here we provide new evidence of a direct role played by the intestinal epithelium, pointing at molecular factors that would need to be balanced to maximize a positive clinical response over the risk of unwanted side effects. In particular, our data suggest that activation of TLR-5 signalling could cooperate with IL-1β and IL-10 to tame down inflammatory responses, likely favouring a productive antitumour response.

Overall, the gut-on-a-chip can be employed to quantitatively investigate the molecular effects associated with bacterial components and to develop them into more effective and safe therapies.

Methods

Cell lines and bacterial strains

Caco-2 cells were obtained from the American Type Culture Collection. HT-29 MTX cells were a gift from G. Monteleone (University of Rome Tor Vergata). Caco-2 cells were cultured in flasks in Eagle's minimal essential medium (EMEM, Merck) supplemented with 20% fetal bovine serum (FBS, Microtech), 10 mM 4-(2-hydroxyethyl)-1-piperazineethanesulfonic acid (HEPES, Sigma-Aldrich), 1 mM sodium pyruvate (Euroclone), 0.1 mM non-essential amino acids (Euroclone), 2 mM L-glutamine (Glu, Euroclone). HT-29 MTX cells were cultured in flasks in Dulbecco's modified Eagle medium (DMEM, Euroclone) supplemented with 10% FBS and 10 mM HEPES. Caco-2 and HT-29 MTX cells were used between passages 10 and 20 and cocultured in Caco-2 medium.

HMEC-1 were obtained from the Center for Disease Control and Prevention. HMEC-1 were cultured in collagen-coated flasks in MCBD 131 medium supplemented with 20% FBS, 10 mM HEPES, 10 mM Glu, 1 mg ml^{-1} hydrocortisone (Euroclone) and 20 ng ml^{-1} human epidermal growth factor (EGF, Gibco). Cells were cultured in a humidified environment at 37 °C in 5% CO_2 between passages 5 and 15.

hiPSCs-derived intestinal organoids

hiPSCs were obtained from The Jackson Laboratory (www.jax.org, KOLF2.1J). Generation of intestinal organoids derived from induced pluripotent stem cells (iPSCs) was performed according to ref. 18 with slight modifications. Briefly, iPSCs were cultured on Vitronectin XF (Stemcell Technologies) coated six-well plates in E8 medium consisting of DMEM F12 with HEPES (Gibco), 128 ng ml^{-1} ascorbic acid (Sigma-Aldrich), 1× insulin–transferrin–selenium (Thermo Fisher Scientific), 10 ng ml^{-1} FGF2 (Peprotech), 500 ng ml^{-1} heparin (Sigma-Aldrich), and 2 ng ml^{-1} TGFβ1 (Peprotech). iPSCs were passaged once a week using ReLeSR dissociation reagent (Stemcell Technologies) when cells reached 80% confluence. For experiments, iPSCs were used between passages 8 and 16.

For intestinal spheroid differentiation, iPSCs were treated with 3 μM CHIR99021 (Sigma-Aldrich) and 100 ng ml^{-1} ActivinA (R&D Systems) in Roswell Park Memorial Institute medium (RPMI) (Gibco catalogue number 11875093) supplemented with 2 mM GlutaMAX (Gibco) and 1× Pen-Strep (Gibco) on day 1, followed by 100 ng ml^{-1} ActivinA in RPMI supplemented with 0.2% FBS (Gibco), 2 mM GlutaMAX and 1× Pen-Strep. The medium was changed daily until day 4. On day 4, cells underwent hindgut differentiation by treatment with 3 μM CHIR99021 and 500 ng ml^{-1} FGF4 (Peprotech) in RPMI supplemented with 1× B27 without ascorbic acid (Gibco), 2 mM GlutaMAX (Gibco) and 1× Pen-Strep (Gibco). The medium was refreshed daily for the next 4 days. Starting on day 8, cells were cultured in Advanced DMEM F12 (Invitrogen) supplemented with 1× B27 (Gibco), 2 mM GlutaMAX (Gibco), 1× Pen-Strep (Gibco), 3 μM CHIR99021, 300 nM LDN193189 (Axon) and 100 ng ml^{-1} EGF (Immunotools). The final medium was labelled as human intestinal organoid (HIO) final medium. The medium was refreshed every 3 days.

On day 20, cells were dissociated to a single-cell solution with Accutase (Stemcell Technologies) for 7 min at 37 °C. The single-cell solution was centrifuged at 350 *g* for 4 min and resuspended in 50 μl Matrigel. The Matrigel containing the cells was plated as a dome in a 24-well plate (Fisher Scientific catalogue number 10380932) and allowed to polymerize for 30 min. Each dome was filled with 1.5 ml of HIO final medium. The medium was refreshed every 3 days, and organoids were passaged every 12 days at a ratio of 1:6. After reaching the desired dimension and morphology (12–14 days), organoids were collected with a syringe tip and dissociated mechanically and enzymatically in 1 ml Tryple Express (Gibco catalogue number 12604013) for 5 min. Dissociated organoids were centrifuged at 350 *g* for 4 min and resuspended in HIO final medium supplemented with 10 μM Y27632 (Rock inhibitor; Selleckchem catalogue number S1049) for injection into the microfluidic device.

Human faecal and blood samples

Faecal material from healthy donors or from patients with melanoma responding and non-responding to immunotherapy were obtained at European Institute of Oncology IRCCS (IEO) before the starting of any treatment. No compensation was paid to patients for participating in the study. All participants and patients gave their informed consent for inclusion before they participated in the study. The studies were conducted in accordance with the Declaration of Helsinki, and the protocols were approved by IEO Ethical Committees (registered as IEO1271 and IEO889, respectively). Serial 10-fold dilutions obtained from 50 mg ml^{-1} faecal matter were plated for 72 h in non-selective Gifu Anaerobic Broth (GAM) agar plates in aerobic and anaerobic conditions to quantify the bacterial load through colony-forming unit counts. For on-chip experiments, faecal samples were suspended in Caco-2 medium at a concentration of 10 mg ml^{-1}.

Blood samples from healthy volunteers were collected at IEO under an approved protocol (IEO 1781).

Gut-on-a-chip preparation

Microfluidic chips were fabricated at Politecnico di Milano (MiMic Lab, Dipartimento di Elettronica Informazione e Bioingegneria) using standard soft lithography techniques. The polydimethylsiloxane device is composed of an intestinal epithelial channel (700 μm wide, 0.65 cm long and 150 μm high) and a microvascular endothelial channel (700 μm wide, 0.65 cm long and 150 μm high) separated by ECM (300 μm wide, 0.65 cm long and 150 μm high). Shield-shaped micropillars (55 μm wide, 100 μm long, 100 μm high, 50 μm spacing) allow the confinement of ECM in the central region. A superimposed actuation chamber (0.3 cm wide, 0.85 cm long and 150 μm high) enables cyclic and controlled deformation of the construct.

The ECM channel was filled with collagen matrix prepared on ice by mixing rat-tail collagen I (final concentration 4.5 mg ml^{-1}, Corning) with PBS10× (10% total volume, Microtech), NaOH (2% collagen volume, Sigma) and double-distilled H_2O.

The pre-mixed Caco-2:HT-29 MTX cell suspension (9:1 ratio, 8×10^6 cells per ml) was seeded on two consecutive days on a pre-coated (200 mg ml^{-1} rat-tail collagen I and 1% Matrigel, Corning) epithelial channel. On the next day, HMEC-1 (10×10^6 cells per ml) were seeded on the pre-coated microvascular endothelial channel and left to adhere to the ECM wall for 24 h. Starting from the third day, the microfluidic devices were connected to a programmable pneumatic actuation system (uBoX, BiomimX Srl) and cultured in mechanically active conditions (deformation 10–15%, frequency 0.2 Hz) up to day 9.

For organoids experiments, disaggregated hiPSCs-derived intestinal organoids were seeded on a pre-coated (200 mg ml^{-1} rat-tail collagen I and 1% Matrigel, Corning) epithelial channel. Starting from day 2, the microfluidic devices were connected to the uBoX system

and cultured in mechanically active conditions (deformation 10–15%, frequency 0.2 Hz) up to day 9.

Intestinal epithelial barrier permeability assay

Gut-on-a-chip devices were prepared as previously described and maintained under mechanically active conditions until day 9 (6 days of actuation). Each chip was microscopically assessed to confirm barrier integrity by injecting TRITC-dextran (4.4 kDa, 1 mg ml^{-1}, Sigma) and FITC-dextran (40 kDa, 1 mg ml^{-1}, Sigma) in the epithelial and microvascular endothelial channels, respectively, and using widefield fluorescence microscope imaging (EVOS FL Cell Imaging System, Invitrogen) every 15 min for up to 1 h. Images were analysed using Fiji (ImageJ, version 2.0.0-rc-59/1.51n). Dextran fluorescence intensity was measured in the lateral channels and in the gel channel, and apparent permeability was calculated as follows:

$$P_{app}\,(\mathrm{cm\,s^{-1}}) = \frac{I_{end} - I_{initial}}{T_{end} - T_{initial}} \times \frac{V_{gel}}{I_0 \times A_{barrier}}$$

where P_{app} is the permeability score in centimetres per second, I_{end} is the fluorescence intensity in the gel channel at the last time point, $I_{initial}$ is the fluorescence intensity in the gel channel at the beginning of the experiment, T_{end} is the last time point in seconds, $T_{initial}$ is the initial time in seconds, I_0 is the fluorescence intensity in the tubule channel at the beginning of the experiment, V_{gel} is the volume of the gel in cubic centimetres and $A_{barrier}$ is the surface area of the tubule that contacts the gel in square centimetres.

To evaluate the response to pro-inflammatory insults, the chip with a mature intestinal epithelial barrier was injected on day 8 with LPSs in the epithelial channel (LPS EC) and incubated in standard culturing conditions for 24 h. Dextran's permeability assay was performed before and at the end of the treatment.

Immunofluorescence microscopy

3D chips were fixed in 4% paraformaldehyde (Electron Microscopy Science) for 30 min at room temperature, washed in PBS for 1 h and thus permeabilized and blocked for 1 h at room temperature (0.25% Triton X-100, 5% FBS, 3% BSA in PBS). All stainings were performed overnight at 4 °C using pre-mixed primary antibodies targeting the following human proteins: ZO-1 (1:100, Invitrogen, catalogue number 339188), E-cadherin (1:200, Abcam, catalogue number ab1416), β-catenin (1:200, BD Bioscience, catalogue number ab8480), villin (1:100, Santa Cruz, catalogue number sc-58897), Ki67 (1:500, Abcam, catalogue number ab15580), cleaved caspase-3 (1:400, Cell Signaling, catalogue number 9661S), MUC2 (1:100, Thermo Fisher, catalogue number MA5-12345), MUC5AC (1:100, Invitrogen, catalogue number MA5-12178), VE-cadherin (1:400, Abcam, catalogue number ab33168) and ICAM-1 (1:250, BD Bioscience, catalogue number VE297946) in dilution buffer (0.1% Triton X-100, 3% BSA in PBS). After 1 h washing at room temperature in dilution buffer, each sample was incubated with the appropriate combination of fluorescently conjugated secondary antibodies (1:500) for 4 h at room temperature. Finally, samples were further washed in PBS and stained for 30 min at room temperature with phalloidin (1:100, Invitrogen, catalogue number 1615008) and DAPI (1:500).

Response to faecal material from healthy donors or patients with melanoma was evaluated at day 8 by adding 10 mg ml^{-1} faecal material diluted in Caco-2 medium on the epithelial barrier for 24 h. To evaluate the response to faecal soluble factors, faecal samples (10 mg ml^{-1} in Caco-2 medium) were centrifuged (1,400 *g*, 5 min) and filtered (0.22 µm) before treatment. LPS from *E. coli* O111:B4 (EC, L2630 Merck), *E. coli* O111:B4 (EB, tlrl-3pelps InvivoGen), *P. gingivalis* (tlrl-ppglps InvivoGen) and *Rhodobacter sphaeroides* (tlrl-prslps InvivoGen) were used at 10 µg ml^{-1}, unless differently indicated. For experiments in anaerobic conditions, faecal sample preparation and the co-culture with complete epithelial constructs (6 h treatment on day 8) were conducted in an anaerobic workstation (A45, Don Whitley Scientific).

To assess potential therapeutic effects, chips were treated at day 8 for 24 h with the indicated combinations of faecal material or soluble factors from non-responsive or responsive patients (each at 5 mg ml^{-1} in Caco-2 medium), LPS EC (10 µg ml^{-1}) or purified flagellin from *S. typhimurium* (100 ng ml^{-1}, Invitrogen).

Confocal laser-scanning microscopy was performed using an Inverted Leica SP8AOBS (Leica). Z-stacks of a minimum of three random fields of view per chip were recorded. Images were analysed and quantified using Fiji (ImageJ, version 2.0.0-rc-59/1.51n).

Mucus layer characterization

To characterize the mucus layer produced by epithelial cells in the gut-on-a-chip devices, Alcian blue/eosin staining was performed. Epithelial cells were washed twice in PBS1× followed by hydration with distilled water, then stained with Alcian blue solution (Alcian blue 8GX Fluka in 3% acetic acid solution) for 45 min at room temperature. Subsequently, a 30 min eosin staining (1:10 Eosin HT110116, Sigma) was performed. Finally, three washing steps with water were performed to remove residual staining. Images were taken in widefield with Leica DM6 B (Histo Fluo) and analysed with ImageJ.

T cells adhesion assay on microvascular endothelial cells

Complete microvascular endothelial tubules (day 5) were stimulated with LPS EC (10 µg ml^{-1}, 24 h) from the epithelial channel and, after LPS removal (day 6), pre-labelled T cells (Calcein, 0.4 µM, Life Technologies) isolated from healthy donors were injected into the microvascular endothelial channel. T cells were allowed to adhere for 30 min and then washed twice with PBS. Fluorescence images (EVOS FL Cell Imaging System, Invitrogen) of the microvascular endothelial channel were taken after injection of T cells and after the second PBS washing.

Total RNA extraction and sequencing

Epithelial cells from gut-on-a-chip devices ($n \geq 3$ for each condition) were collected at day 9 post treatment, flushing trypsin-EDTA solution (Euroclone) in the channels and incubating the device for 10–20 min at 37 °C. Collected pellets were centrifuged, resuspended in 350 µl of freezing solution (40 mM dithiothreitol solution (Merck) in RLT buffer (Qiagen)) and stored at −80 °C until further processing. RNA was extracted using RNeasy Mini Kit (Qiagen catalogue number 74106), and on-column digestion DNA was performed using RNAse-Free DNase Set (Qiagen catalogue number 79254) following manufacturer's instructions. RNA was eluted in 50 µl of RNAse-Free water. Sample quality and quantity were checked by Bioanalyzer and Qubit, respectively. Ribosomal RNA was depleted with Ribo-Zero rRNA Removal Kit and efficiency checked with Bioanalyzer 2100.

RNA sequencing libraries were prepared with Illumina TruSeq Stranded Total RNA kit following the manufacturer's protocol. Briefly, after the fragmentation of RNA, complementary DNA was synthesized, end-repaired and 3′-end adenylated. Following adapter ligation, libraries were amplified by PCR. Amplified libraries were checked on Bioanalyzer 2100 and quantified with PicoGreen reagent. Libraries with distinct TruSeq adapter indexes were multiplexed and, after cluster generation on FlowCell, were sequenced for 50 bases in the paired-end mode on a Novaseq 6000 sequencer. Base calling was performed in real time during the Novaseq runs by Real-Time Analysis v3.4.4 (RTA, Illumina) software.

RNAseq data analysis

Generated raw paired-end reads were subjected to quality check using FastQC v0.11.9 to identify the base quality score, adapters and ambiguity reads[83]. Furthermore, on the basis of quality check, the reads were trimmed using Trimmomatic v0.39[84]. STAR aligner v2.7.10a was used to map the high-quality trimmed read to the reference genome GRCh38 for annotation[85]. Mapped reads were quantified using featurecounts

v2.0.2 to generate the count matrix of each comparison[85]. Differential expression analysis was performed using edgeR v4.2.3, and the read counts <5 in all samples were removed before downstream analysis[86]. The remaining reads were transformed to log count per million values to perform PCA using the top 4,000 variable genes before and after considering the batch effect. The PCA was calculated using R base prcomp v4.3.1, and the plots to identify the batch effect was generated using ggplot2 v3.4.1[87]. To obtain the DEGs, the log count per million values were subjected to limma-voom pipeline v3.52.4. DEGs were filtered using $P < 0.01$ and were subjected to functional profiling using clusterProfiler v4.6.2 9 (ref. 88).

To perform the upstream analysis and visualization, NetworkAnalyst v3 was used to identify the interactions between the transcription factor and genes[89]. The list of DEGs were mapped to the Kyoto Encyclopedia of Genes and Genomes database using Cytoscape ClueGo plugin, and the interaction between transcription factor and significant pathways were highlighted in the transcription factor–gene interaction network[90]. The enrichment analysis was performed on metascape online system with default parameters (minimum overlap 3, minimum enrichment 1.5, *P* value threshold) (https://metascape.org/gp/index.html). A set of significant DEGs was used for pathway and functional enrichment analyses using databases such as Kyoto Encyclopedia of Genes and Genomes pathway, GO, reactome, hallmark gene set and canonical pathway. Specifically, *P* values were calculated based on accumulative hypergeometric distribution[90].

Correlation between human–mouse orthologous in vivo and chip model

Laser microdissection epithelial normalized mouse data of six conventional and six germ-free mice were used to perform the GSEA enrichment[91]. For duplicate genes with different expression values, the mean expression value was selected separately for conventional and germ-free mice. To perform the GSEA, gmt files were constructed using the significant GO terms ($q < 0.01$) enriched in the faecal microbiome and used as a reference. The GSEA enriched terms were matched, separately to all up and down GO enriched terms from faeces. The resultant list of terms was filtered out using the enrichment score of >0.5 and <−0.4. A contingency table was constructed, and two-tailed chi-square test was performed on the filtered human–mouse orthologous enriched terms.

qPCR assays

About 1 µg of total RNA was retro-transcribed with MultiScribe Reverse Transcriptase in 20 µl following manufacturer's instructions (High-Capacity cDNA Reverse Transcription Kit, Thermo Fisher). cDNA (5 ng µl^{-1}) was used as template in 20 µl qPCR reaction mix containing SSoFast EvaGreen Supermix (BioRad) loaded on a Fast 96-Well Reaction plate (Applied Biosystems). qPCR was then run on a QuantStudio 6 Pro System (Thermo Fisher) using the following protocol: one cycle of 2 min at 95 °C, followed by 40 cycles of a two-stage temperature profile of 95 °C for 30 s and optimal melting temperature T_m (60 °C) for 30 s. A melting curve phase was added with a first cycle of 95 °C for 1 s and two-stage temperature of 60 °C for 20 s and a ramp rate of 0.10 °C s^{-1} up to 95 °C. Primers used in the qPCR assays are listed in Supplementary Table 1. Quantification cycle (Cq) values were retrieved from Thermo Fisher Connect online system. GAPDH gene was used as reference house-keeping to calculate the ΔCq values. A negative control was used as reference sample in all the qPCR assays performed, to get a relative gene quantification adopting the $2^{-\Delta\Delta Cq}$ formula[46,92]. Efficacy of primers was evaluated by performing a standard curve analysis using ten serial dilutions of the reference sample.

Bead-based multiplexed ELISA

Multiplexed ELISA on chip cultured media were performed on a Luminex 200 platform (Luminex) using custom kits of pre-mixed antibody-coated beads (R&D Systems), which included the following analytes: IL-1β, IL-6, CXCL8, VEGF, CCL20, TNF and IFNγ. Briefly, based on manufacturer's instructions, 50 µl of media and kit standards were added to each well and incubated with a diluted microparticle cocktail at 4 °C, overnight, on a shaker (Thermomixer compact) at 850 r.p.m. After washing the unbound soluble molecules, the biotin–antibody cocktail specific to the analytes of interest was added to each well for 1 h at room temperature. Wells were washed again, and conjugated streptavidin–phycoeriythrin was added for 30 min at room temperature. After washing, microparticles were resuspended in the provided washing buffer and read on a Luminex 200 platform. The outputs (pg ml^{-1}) were visualized and statistically analysed in Prism (version 10).

Shotgun sequencing and analyses

Fresh faecal samples from patients with melanoma were submitted for Shotgun metagenomic sequencing at the Next-Generation Sequencing Core Facility of University of Trento. Metagenomic sequence data were run through the biobakery 3 pipeline (MetaPhlAn 4.0.3 vJan21-CHOCOPhlAnSGB 202103; HUMAnN v3.6 vJan21-CHOCOPhlAnSGB 202103), which leverages a set of 99,200 high-quality and fully annotated reference microbial genomes spanning 16,800 species and 87.3 million UniRef90 functional annotations available in UniProt as of January 2019. Taxonomic profiling of taxa composition of all metagenomic samples was performed with MetaPhlAn v4.0.3[93] using default parameters and CHOCOPhlAnSGB v202103 as database. Functional potential analysis of the metagenomic samples was performed with HUMAnN v3.6[94] using default parameters.

To determine significantly differentially abundant taxa, Wilcoxon rank sum test was performed on taxonomic abundance data from metaphlan (relative abundance), with *P* value adjustment by false discovery rate. To determine the group with which a feature was associated, the corresponding $\log_2$ fold change was also computed, by adding an offset of 0.01 to the abundances, getting the mean relative abundance of each feature across samples within a group and, using the foldchange v3.9.5 package, getting the fold change (gtools)[95] of the group means and converting it to log-ratio (foldchange2logratio).

Per-sample taxa abundances were visualized using ComplexHeatmap v2.8.0 (ref. 96).

To evaluate the functional potential of LPS synthesis, we focused on the relative abundances of UniRef90 obtained from HUMAnN v3.6[14] that were annotated to the LPS biosynthesis Keyword (KW-0448) in UniProt. In June 2023, this keyword contained a total of 118,650 entries. For visualization and statistical analysis, we utilized the ggplot2 v3.4.2[97] and ggpubr v0.6.0[98] packages in R v4.2.3, respectively.

Reporting summary

Further information on research design is available in the Nature Portfolio Reporting Summary linked to this article.

Data availability

The generated transcriptomic data are available via Zenodo at https://doi.org/10.5281/zenodo.13889913 (ref. 99). The raw sequence data are available with accession number E-MTAB-13312 on the Annotare 2.0, ArrayExpress database at https://www.ebi.ac.uk/biostudies/arrayexpress. The raw and analysed datasets generated during the study are available for research purposes from the corresponding author on reasonable request.

Code availability

The code to generate the plots is available via GitHub at https://github.com/Punit201016/Gut_on_Chip.

References

1. Larkin, J. et al. Efficacy and safety of nivolumab in patients with BRAF V600 mutant and BRAF wild-type advanced melanoma: a pooled analysis of 4 clinical trials. *JAMA Oncol.* **1**, 433–440 (2015).

2. Schadendorf, D. et al. Pooled analysis of long-term survival data from phase II and phase III trials of ipilimumab in unresectable or metastatic melanoma. *J. Clin. Oncol.* **33**, 1889–1894 (2015).
3. Ribas, A. et al. Association of pembrolizumab with tumor response and survival among patients with advanced melanoma. *JAMA* **315**, 1600–1609 (2016).
4. Robert, C. et al. Pembrolizumab versus ipilimumab in advanced melanoma (KEYNOTE-006): post-hoc 5-year results from an open-label, multicentre, randomised, controlled, phase 3 study. *Lancet Oncol.* **20**, 1239–1251 (2019).
5. Robert, C. et al. Pembrolizumab versus ipilimumab in advanced melanoma. *N. Engl. J. Med.* **372**, 2521–2532 (2015).
6. Robert, C. et al. Nivolumab in previously untreated melanoma without BRAF mutation. *N. Engl. J. Med.* **372**, 320–330 (2015).
7. Pardoll, D. M. The blockade of immune checkpoints in cancer immunotherapy. *Nat. Rev. Cancer* **12**, 252–264 (2012).
8. Wykes, M. N. & Lewin, S. R. Immune checkpoint blockade in infectious diseases. *Nat. Rev. Immunol.* **18**, 91–104 (2017).
9. Sharma, P., Hu-Lieskovan, S., Wargo, J. A. & Ribas, A. Primary, adaptive and acquired resistance to cancer immunotherapy. *Cell* **168**, 707–723 (2017).
10. Johnson, D. B., Nebhan, C. A., Moslehi, J. J. & Balko, J. M. Immune-checkpoint inhibitors: long-term implications of toxicity. *Nat. Rev. Clin. Oncol.* **19**, 254–267 (2022).
11. Morad, G., Helmink, B. A., Sharma, P. & Wargo, J. A. Hallmarks of response, resistance, and toxicity to immune checkpoint blockade. *Cell* **184**, 5309–5337 (2021).
12. Gopalakrishnan, V. et al. Gut microbiome modulates response to anti-PD-1 immunotherapy in melanoma patients. *Science* **359**, 97–103 (2018).
13. Matson, V. et al. The commensal microbiome is associated with anti-PD-1 efficacy in metastatic melanoma patients. *Science* **359**, 104–108 (2018).
14. Routy, B. et al. Gut microbiome influences efficacy of PD-1-based immunotherapy against epithelial tumors. *Science* **359**, 91–97 (2018).
15. Frankel, A. E. et al. Metagenomic shotgun sequencing and unbiased metabolomic profiling identify specific human gut microbiota and metabolites associated with immune checkpoint therapy efficacy in melanoma patients. *Neoplasia* **19**, 848–855 (2017).
16. Bäckhed, F., Ley, R. E., Sonnenburg, J. L., Peterson, D. A. & Gordon, J. I. Host-bacterial mutualism in the human intestine. *Science* **307**, 1915–1920 (2005).
17. Gill, S. R. et al. Metagenomic analysis of the human distal gut microbiome. *Science* **312**, 1355–1359 (2006).
18. Cresci, G. A. M. & Izzo, K. in *Adult Short Bowel Syndrome: Nutritional, Medical, and Surgical Management* (eds Corrigan, M. L.) 45–54 (Academic, 2019); https://doi.org/10.1016/B978-0-12-814330-8.00004-4
19. Litvak, Y. & Bäumler, A. J. Microbiota-nourishing immunity: a guide to understanding our microbial self. *Immunity* **51**, 214–224 (2019).
20. Ma, W. et al. Dietary fiber intake, the gut microbiome, and chronic systemic inflammation in a cohort of adult men. *Genome Med.* **13**, 102 (2021).
21. Kho, Z. Y. & Lal, S. K. The human gut microbiome—a potential controller of wellness and disease. *Front. Microbiol.* **9**, 356589 (2018).
22. Pickard, J. M., Zeng, M. Y., Caruso, R. & Núñez, G. Gut microbiota: role in pathogen colonization, immune responses, and inflammatory disease. *Immunol. Rev.* **279**, 70–89 (2017).
23. McCulloch, J. A. et al. Intestinal microbiota signatures of clinical response and immune-related adverse events in melanoma patients treated with anti-PD-1. *Nat. Med.* **28**, 545–556 (2022).
24. Hugenholtz, F. & de Vos, W. M. Mouse models for human intestinal microbiota research: a critical evaluation. *Cell. Mol. Life Sci.* **75**, 149–160 (2018).
25. Xiang, Y. et al. Gut-on-chip: recreating human intestine in vitro. *J. Tissue Eng.* **11**, 2041731420965318 (2020).
26. Nguyen, T. L. A., Vieira-Silva, S., Liston, A. & Raes, J. How informative is the mouse for human gut microbiota research? *Dis. Model. Mech.* **8**, 1–16 (2015).
27. Nagpal, R. et al. Comparative microbiome signatures and short-chain fatty acids in mouse, rat, non-human primate, and human feces. *Front. Microbiol.* **9**, 413720 (2018).
28. Sato, T. & Clevers, H. Growing self-organizing mini-guts from a single intestinal stem cell: mechanism and applications. *Science* **340**, 1190–1194 (2013).
29. Kim, H. J., Huh, D., Hamilton, G. & Ingber, D. E. Human gut-on-a-chip inhabited by microbial flora that experiences intestinal peristalsis-like motions and flow. *Lab Chip* **12**, 2165–2174 (2012).
30. Kim, H. J., Li, H., Collins, J. J. & Ingber, D. E. Contributions of microbiome and mechanical deformation to intestinal bacterial overgrowth and inflammation in a human gut-on-a-chip. *Proc. Natl Acad. Sci. USA* **113**, E7–E15 (2016).
31. Whitesides, G. M. The origins and the future of microfluidics. *Nature* **442**, 368–373 (2006).
32. Beebe, D. J., Mensing, G. A. & Walker, G. M. Physics and applications of microfluidics in biology. *Annu. Rev. Biomed. Eng.* **4**, 261–286 (2002).
33. Sackmann, E. K., Fulton, A. L. & Beebe, D. J. The present and future role of microfluidics in biomedical research. *Nature* **507**, 181–189 (2014).
34. Moossavi, S., Arrieta, M. C., Sanati-Nezhad, A. & Bishehsari, F. Gut-on-chip for ecological and causal human gut microbiome research. *Trends Microbiol.* **30**, 710–721 (2022).
35. Nitsche, K. S., Müller, I., Malcomber, S., Carmichael, P. L. & Bouwmeester, H. Implementing organ-on-chip in a next-generation risk assessment of chemicals: a review. *Arch. Toxicol.* **96**, 711–741 (2022).
36. Marsano, A. et al. From chip-in-a-lab to lab-on-a-chip: towards a single handheld electronic system for multiple application-specific lab-on-a-chip (ASLOC). *Lab Chip* **14**, 2168–2176 (2014).
37. Occhetta, P. et al. Hyperphysiological compression of articular cartilage induces an osteoarthritic phenotype in a cartilage-on-a-chip model. *Nat. Biomed. Eng.* **3**, 545–557 (2019).
38. Ades, E. W. et al. HMEC-1: establishment of an immortalized human microvascular endothelial cell line. *J. Invest. Dermatol.* **99**, 683–690 (1992).
39. Spence, J. R. et al. Directed differentiation of human pluripotent stem cells into intestinal tissue in vitro. *Nature* **470**, 105–109 (2011).
40. Shi, Y., Inoue, H., Wu, J. C. & Yamanaka, S. Induced pluripotent stem cell technology: a decade of progress. *Nat. Rev. Drug Discov.* **16**, 115–130 (2017).
41. Kasendra, M. et al. Development of a primary human Small Intestine-on-a-Chip using biopsy-derived organoids. *Nature* **8**, 2871 (2018).
42. Workman, M. J. et al. Enhanced utilization of induced pluripotent stem cell-derived human intestinal organoids using microengineered chips. *Cell Mol. Gastroenterol. Hepatol.* **5**, 669–677.e2 (2018).
43. Crawley, S. W. et al. Intestinal brush border assembly driven by protocadherin-based intermicrovillar adhesion. *Cell* **157**, 433–446 (2014).
44. Lesuffleur, T. et al. Growth adaptation to methotrexate of HT-29 human colon carcinoma cells is associated with their ability to differentiate into columnar absorptive and mucus-secreting cells. *Cancer Res.* **50**, 6334–6343 (1990).

45. Sommer, F., Nookaew, I., Sommer, N., Fogelstrand, P. & Bäckhed, F. Site-specific programming of the host epithelial transcriptome by the gut microbiota. *Genome Biol.* **16**, 62 (2015).
46. Morgun, A. et al. Uncovering effects of antibiotics on the host and microbiota using transkingdom gene networks. *Gut* **64**, 1732–1743 (2015).
47. Vétizou, M. et al. Anticancer immunotherapy by CTLA-4 blockade relies on the gut microbiota. *Science* **350**, 1079–1084 (2015).
48. Lee, K. A. et al. Cross-cohort gut microbiome associations with immune checkpoint inhibitor response in advanced melanoma. *Nat. Med.* **28**, 535–544 (2022).
49. Davar, D. et al. Fecal microbiota transplant overcomes resistance to anti–PD-1 therapy in melanoma patients. *Science* **371**, 595–602 (2021).
50. Baruch, E. N. et al. Fecal microbiota transplant promotes response in immunotherapy-refractory melanoma patients. *Science* **371**, 602–609 (2021).
51. Routy, B. et al. Fecal microbiota transplantation plus anti-PD-1 immunotherapy in advanced melanoma: a phase I trial. *Nat. Med.* **29**, 2121–2132 (2023).
52. Lin, D. P., Jin, Y. L., Hu, D. Y., Ying, S. J. & Jiang, Y. Influence of TRAIL deficiency on Th17 cells and colonic microbiota in experimental colitis mouse model. *Am. J. Med Sci.* **362**, 188–197 (2021).
53. Meng, X., Zhang, J., Wu, H., Yu, D. & Fang, X. *Akkermansia muciniphila* aspartic protease Amuc_1434* inhibits human colorectal cancer LS174T cell viability via TRAIL-mediated apoptosis pathway. *Int. J. Mol. Sci.* **21**, 3385 (2020).
54. Davison, J. M. et al. Microbiota regulate intestinal epithelial gene expression by suppressing the transcription factor hepatocyte nuclear factor 4 alpha. *Genome Res.* **27**, 1195–1206 (2017).
55. Heppert, J. K. et al. Transcriptional programmes underlying cellular identity and microbial responsiveness in the intestinal epithelium. *Nat. Rev. Gastroenterol. Hepatol.* **18**, 7–23 (2020).
56. Camp, J. G. et al. Microbiota modulate transcription in the intestinal epithelium without remodeling the accessible chromatin landscape. *Genome Res.* **24**, 1504 (2014).
57. Dey, N. et al. Regulators of gut motility revealed by a gnotobiotic model of diet-microbiome interactions related to travel. *Cell* **163**, 95–107 (2015).
58. Fernandes, M. R., Aggarwal, P., Costa, R. G. F., Cole, A. M. & Trinchieri, G. Targeting the gut microbiota for cancer therapy. *Nat. Rev. Cancer* **22**, 703–722 (2022).
59. Angrisano, T. et al. LPS-induced IL-8 activation in human intestinal epithelial cells is accompanied by specific histone H3 acetylation and methylation changes. *BMC Microbiol.* **10**, 172 (2010).
60. Herath, T. D. K. et al. Tetra- and penta-acylated lipid A structures of *Porphyromonas gingivalis* LPS differentially activate TLR4-mediated NF-κB signal transduction cascade and immuno-inflammatory response in human gingival fibroblasts. *PLoS ONE* **8**, e58496 (2013).
61. Berezow, A. B. et al. The structurally similar, penta-acylated lipopolysaccharides of *Porphyromonas gingivalis* and *Bacteroides* elicit strikingly different innate immune responses. *Microb. Pathog.* **47**, 68–77 (2009).
62. Steimle, A., Autenrieth, I. B. & Frick, J. S. Structure and function: lipid A modifications in commensals and pathogens. *Int. J. Med. Microbiol.* **306**, 290–301 (2016).
63. DeFilipp, Z. et al. Drug-resistant *E. coli* bacteremia transmitted by fecal microbiota transplant. *N. Engl. J. Med.* **381**, 2043–2050 (2019).
64. Qin, L. et al. p120 modulates LPS-induced NF-κB activation partially through RhoA in bronchial epithelial cells. *BioMed. Res. Int.* **2014**, 932340 (2014).
65. Sarhan, S., Knodgen, B. & Seiler, N. The gastrointestinal tract as polyamine source for tumor growth. *Anticancer Res.* **9**, 215–223 (1989).
66. Pei, Z., Lin, D., Song, X., Li, H. & Yao, H. TLR4 signaling promotes the expression of VEGF and TGFβ1 in human prostate epithelial PC3 cells induced by lipopolysaccharide. *Cell Immunol.* **254**, 20–27 (2008).
67. Cario, E. et al. Lipopolysaccharide activates distinct signaling pathways in intestinal epithelial cell lines expressing Toll-like receptors. *J. Immunol.* **164**, 966–972 (2000).
68. Fontana, M. F. et al. JUNB is a key transcriptional modulator of macrophage activation. *J. Immunol.* **194**, 177–186 (2015).
69. Rawat, M. et al. IL1B increases intestinal tight junction permeability by up-regulation of MIR200C-3p, which degrades occludin mRNA. *Gastroenterology* **159**, 1375–1389 (2020).
70. Wu, W. J. H. et al. Interleukin-1β secretion induced by mucosa-associated gut commensal bacteria promotes intestinal barrier repair. *Gut Microbes* **14**, 2014772 (2022).
71. Seo, S. U. et al. Distinct commensals induce interleukin-1β via NLRP3 inflammasome in inflammatory monocytes to promote intestinal inflammation in response to injury. *Immunity* **42**, 744–755 (2015).
72. Carvalho, F. A., Aitken, J. D., Gewirtz, A. T. & Vijay-Kumar, M. TLR5 activation induces secretory interleukin-1 receptor antagonist (sIL-1Ra) and reduces inflammasome-associated tissue damage. *Mucosal Immunol.* **4**, 102–111 (2011).
73. Carvalho, F. A. et al. Interleukin-1β (IL-1β) promotes susceptibility of Toll-like receptor 5 (TLR5) deficient mice to colitis. *Gut* **61**, 373–384 (2012).
74. Scheithauer, T. P. M. et al. Compensatory intestinal antibody response against pro-inflammatory microbiota after bariatric surgery. *Gut Microbes* **14**, 2031696 (2022).
75. Trietsch, S. J. et al. Membrane-free culture and real-time barrier integrity assessment of perfused intestinal epithelium tubes. *Nat. Commun.* **8**, 262 (2017).
76. Gjorevski, N. et al. Neutrophilic infiltration in organ-on-a-chip model of tissue inflammation. *Lab Chip* **20**, 3365–3374 (2020).
77. Amaria, R. N. et al. Neoadjuvant immune checkpoint blockade in high-risk resectable melanoma. *Nat. Med.* **24**, 1649–1654 (2018).
78. Halsey, T. M. et al. Microbiome alteration via fecal microbiota transplantation is effective for refractory immune checkpoint inhibitor-induced colitis. *Sci. Transl. Med.* **15**, eabq4006 (2023).
79. Andrews, M. C. et al. Gut microbiota signatures are associated with toxicity to combined CTLA-4 and PD-1 blockade. *Nat. Med.* **27**, 1432–1441 (2021).
80. Wang, G. et al. Bacteria induce skin regeneration via IL-1β signaling. *Cell Host Microbe* **29**, 777–791.e6 (2021).
81. Jung, Y. et al. IL-1β in eosinophil-mediated small intestinal homeostasis and IgA production. *Mucosal Immunol.* **8**, 930–942 (2015).
82. Ganesh, B. B. et al. IL-1β promotes TGF-β1 and IL-2 dependent Foxp3 expression in regulatory T cells. *PLoS ONE* **6**, e21949 (2011).
83. Andrews, S. FastQC: a quality control tool for high throughput sequence data. *Babraham Bioinformatics* http://www.bioinformatics.babraham.ac.uk/projects/fastqc/ (2010).
84. Bolger, A. M., Lohse, M. & Usadel, B. Trimmomatic: a flexible trimmer for Illumina sequence data. *Bioinformatics* **30**, 2114–2120 (2014).
85. Dobin, A. et al. STAR: ultrafast universal RNA-seq aligner. *Bioinformatics* **29**, 15–21 (2013).
86. Liao, Y., Smyth, G. K. & Shi, W. featureCounts: an efficient general purpose program for assigning sequence reads to genomic features. *Bioinformatics* **30**, 923–930 (2014).

87. Robinson, M. D., McCarthy, D. J. & Smyth, G. K. edgeR: a Bioconductor package for differential expression analysis of digital gene expression data. *Bioinformatics* **26**, 139–140 (2010).
88. Wickham, H. *ggplot2* (Springer, 2016); https://doi.org/10.1007/978-3-319-24277-4
89. Wu, T. et al. clusterProfiler 4.0: a universal enrichment tool for interpreting omics data. *Innovation* **2**, 100141 (2021).
90. Zhou, G. et al. NetworkAnalyst 3.0: a visual analytics platform for comprehensive gene expression profiling and meta-analysis. *Nucleic Acids Res.* **47**, W234–W241 (2019).
91. Bindea, G. et al. ClueGO: a Cytoscape plug-in to decipher functionally grouped gene ontology and pathway annotation networks. *Bioinformatics* **25**, 1091–1093 (2009).
92. Livak, K. J. & Schmittgen, T. D. Analysis of relative gene expression data using real-time quantitative PCR and the 2−ΔΔCT method. *Methods* **25**, 402–408 (2001).
93. Schmittgen, T. D. et al. Quantitative reverse transcription–polymerase chain reaction to study mRNA decay: comparison of endpoint and real-time methods. *Anal. Biochem.* **285**, 194–204 (2000).
94. Blanco-Míguez, A. et al. Extending and improving metagenomic taxonomic profiling with uncharacterized species using MetaPhlAn 4. *Nat. Biotechnol.* **41**, 1633–1644 (2023).
95. Beghini, F. et al. Integrating taxonomic, functional, and strain-level profiling of diverse microbial communities with bioBakery 3. *eLife* **10**, e65088 (2021).
96. Warnes, G. R., Bolker, B., Lumley, T. & Warnes, M. G. R. Package 'gtools'. R Package version, **3**(1) https://cran.r-project.org/web/packages/gtools/index.html (2015).
97. Gu, Z. Complex heatmap visualization. *iMeta* **1**, e43 (2022).
98. Kassambara, A. ggpubr: 'ggplot2' based publication ready plots. R package version 0.6.0 https://rpkgs.datanovia.com/ggpubr/ (2023).
99. European Institute of Oncology & Tyagi, P. Transcriptomic profile of a MECHANICALLY ACTIVE 3D GUT-ON-CHIP exposed to human FECAL MICROBIOME. *Zenodo* https://doi.org/10.5281/zenodo.13889913 (2024).

Acknowledgements

We thank patients involved in the study and their families, the IEO's Biobank (B4Me), the Genomic Unit, Cell culture Unit and the Imaging Unit (in particular S. Rodighiero and C. Soriani) at IEO for their technical assistance. The silicon wafer micropatterning was performed at PoliFAB, the micro- and nanofabrication facility of Politecnico di Milano. The device design was kindly provided by BiomimX Srl. L.N. thanks TL2 for their support and insightful discussions and dedicates this work to the memory of Roberto di Biase and Alberto Iannuzzi. M.B. is supported by Associazione Italiana per la Ricerca contro il Cancro (AIRC) to L.N. P.T. is supported by Worldwide Cancer Research (WWCR 22-0402) to L.N. C.C. is supported by Fondazione Umberto Veronesi. S.G. is supported by Credit Agricole through Fondazione IEO-CCM. A.M. received DK107603-NIH funding. M.D. is supported by an ERC Consolidator Grant (PD-GUT 101003329), Fondation De France (00147852/WB-2023-51647). H.R. is supported by a Paris Cite' University scholarship (BioSPC DGNRV). This work was supported by AIRC (AIRC IG 26406 to L.N., AIRC StartUp Grant 21474 to T.M.). This project received funding from the European Union's Horizon 2020 research and innovation program under the Marie Skłodowska–Curie grant agreement number 860715. This work was partially supported by the Italian Ministry of Health with Ricerca Corrente and 5x1000 funds.

Author contributions

M.B., M.R. and L.N. designed the study; M.B., S.G., C.C., H.R. and K.K.K. performed the experiments; M.B., S.G., C.C., A.C., B.I.S. and M.F. processed samples; M.B., P.T., C.C., S.G., A.N., A.D.G.M. and L.N. analysed data; A.V., P.O., J.A.W., N.S., A.M., M.D. and T.M. provided critical expertise and resources; P.F.F. and E.C. obtained samples from patients; L.N. coordinated the whole study; M.B. and L.N. wrote and edited the paper. All the authors discussed and read the paper.

Competing interests

M.R. and P.O. are founders and shareholders of BiomimX Srl. The other authors declare no competing interests.

Additional information

Extended data is available for this paper at https://doi.org/10.1038/s41551-024-01318-z.

Supplementary information The online version contains supplementary material available at https://doi.org/10.1038/s41551-024-01318-z.

Correspondence and requests for materials should be addressed to Luigi Nezi.

Peer review information *Nature Biomedical Engineering* thanks Sasan Jalili and the other, anonymous, reviewer(s) for their contribution to the peer review of this work.

Reprints and permissions information is available at www.nature.com/reprints.

Publisher's note Springer Nature remains neutral with regard to jurisdictional claims in published maps and institutional affiliations.

[1]Department of Experimental Oncology, Istituto Europeo di Oncologia – IRCCS (IEO), Milan, Italy. [2]Department of Electronics, Information and Bioengineering, Politecnico di Milano, Milan, Italy. [3]Mechanisms and Therapy of Genetic Brain Diseases, Institut Imagine, INSERM UMR1163, Université Paris Cité, Paris, France. [4]Department of Surgical Oncology, Division of Surgery and Department of Genomic Medicine, Division of Cancer Medicine, The University of Texas MD Anderson Cancer Center, Houston, TX, USA. [5]Dipartimento di Oncologia Interpresidio Gruppo Multimedica IRCCS, Milan, Italy. [6]Humanitas-Gavazzeni, Medical Oncology, Bergamo, Italy. [7]Department CIBIO, University of Trento, Trento, Italy. [8]College of Pharmacy, Oregon State University, Corvallis, OR, USA. [9]Department of Molecular Biotechnology and Health Sciences, University of Torino, Turin, Italy. ✉e-mail: luigi.nezi@ieo.it

https://doi.org/10.1038/s41551-024-01318-z

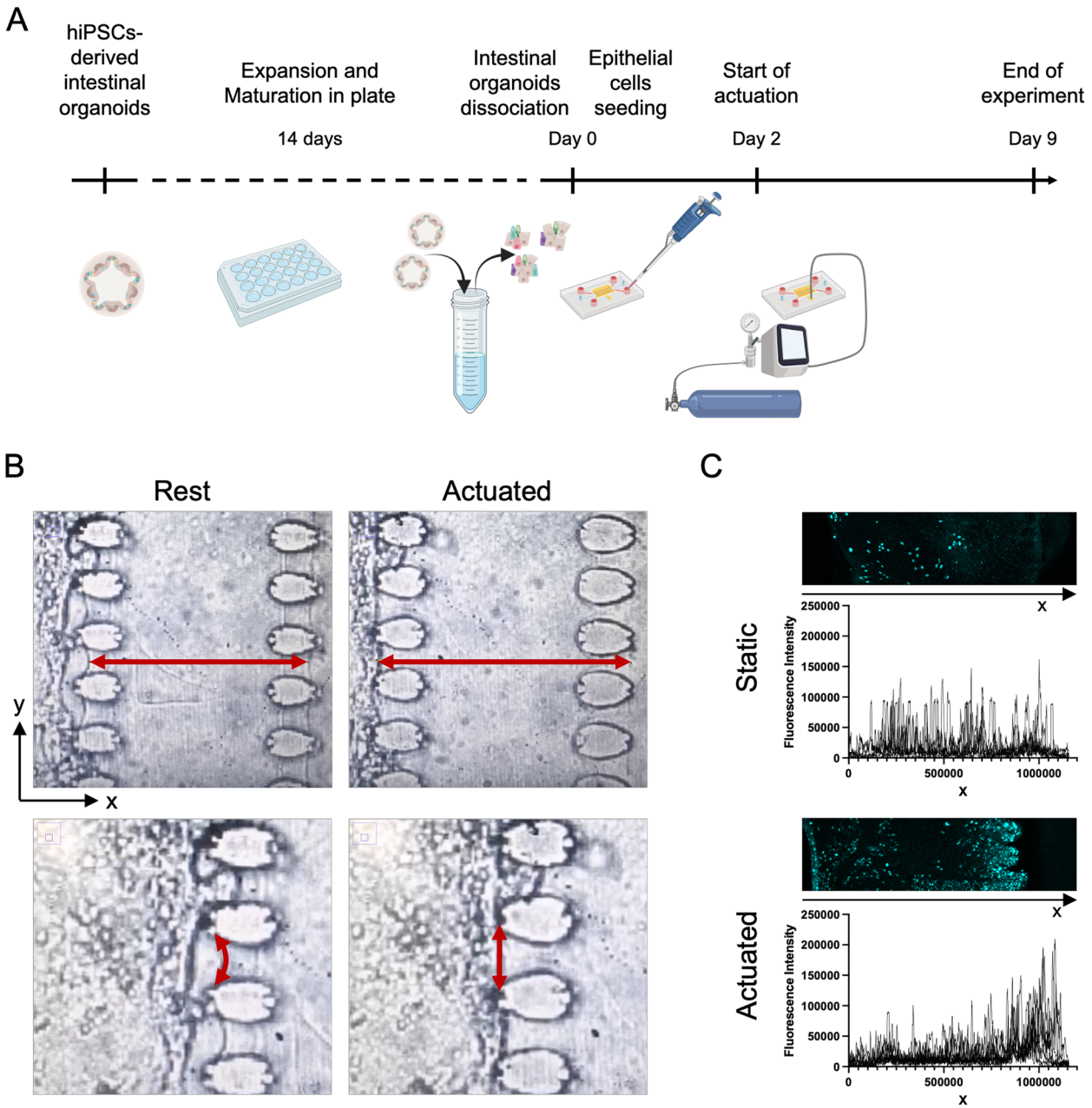

Extended Data Fig. 1 | Human iPSC-derived intestinal organoids. A) Schematic representation of the experimental plan. **B)** Characterization of mechanical actuation. Representative brightfield images of the Gut-on-Chip device in rest and actuated conditions. % Strain of the hydrogel walls (arrows) was calculated in both X and Y directions. **C)** Spatial distribution of proliferative cells (Ki-67) in static and actuated chips seeded with intestinal cells obtained from disaggregated human iPSCs-derived intestinal organoids (Day 9).

https://doi.org/10.1038/s41551-024-01318-z

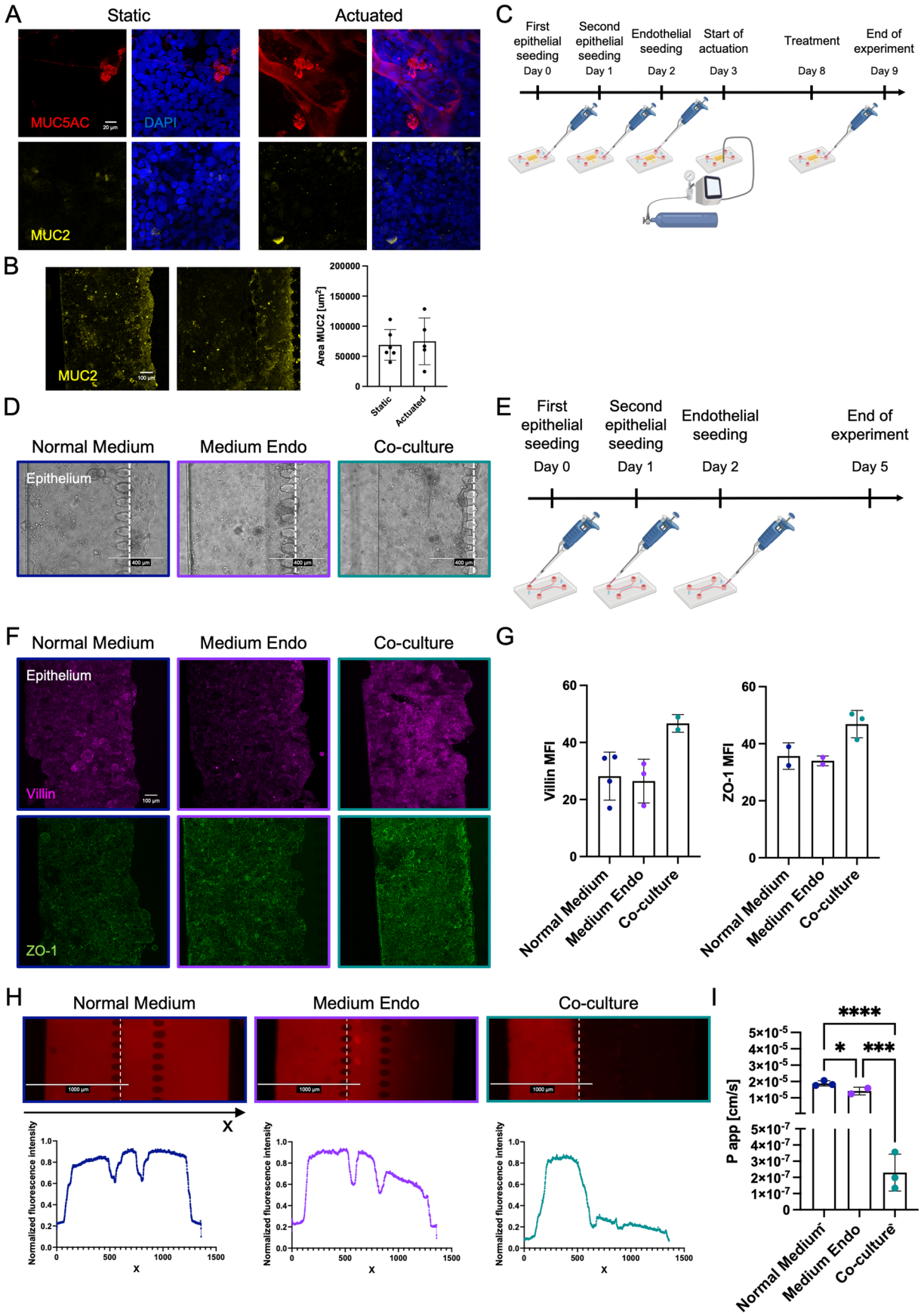

Extended Data Fig. 2 | See next page for caption.

https://doi.org/10.1038/s41551-024-01318-z

Extended Data Fig. 2 | Influence of endothelium on the intestinal epithelium in the chip. A) Representative high-magnification fluorescence microscopy images of MUC5AC (red) and MUC2 (yellow) produced by Caco-2 and HT-29 MTX co-culture in static vs actuated chips. **B)** Fluorescence microscopy images and quantification of MUC2 production in static (n = 6) vs actuated (n = 5) chips. **C)** Schematic representation of the experimental plan. **D)** Bright field images of epithelial cells cultured in normal epithelial medium, endothelial medium (Medium Endo) and in presence of endothelial cells (Co-culture). **E)** Schematic representation of the experimental plan. **F)** Fluorescence microscopy images of villin (magenta) and ZO-1 (green) on epithelial cells cultured in normal epithelial medium, endothelial medium (Medium Endo) and in presence of endothelial cells (Co-culture). **G)** Mean fluorescent intensity (MFI) quantification of villin ($n_{Normal\ Medium}$ = 4, $n_{Medium\ Endo}$ = 2, $n_{Co\text{-}culture}$ = 2) and ZO-1 ($n_{Normal\ Medium}$ = 2, $n_{Medium\ Endo}$ = 2, $n_{Co\text{-}culture}$ = 3) on epithelial cells cultured in normal epithelial medium, endothelial medium (Medium Endo) and in presence of endothelial cells (Co-culture). **H)** Fluorescence microscopy images and normalized fluorescent intensity profile of dextran permeability assay (TRITC Dextran 4.4kDa) on epithelial cells cultured in normal epithelial medium, endothelial medium (Medium Endo) and in presence of endothelial cells (Co-culture). Data were normalized on maximum value. **I)** Apparent permeability (Papp) quantification of epithelial barrier in presence or absence of endothelial cells. ($n_{Normal\ Medium}$ = 3, $n_{Medium\ Endo}$ = 2, $n_{Co\text{-}culture}$ = 3, p = 0.000047 for Co-culture vs Normal Medium, p = 0.0407 for Normal Medium vs Medium Endo, p = 0.0003 for Co-culture vs Medium Endo). Bars represent mean ± SD, ordinary one-way ANOVA (I).

https://doi.org/10.1038/s41551-024-01318-z

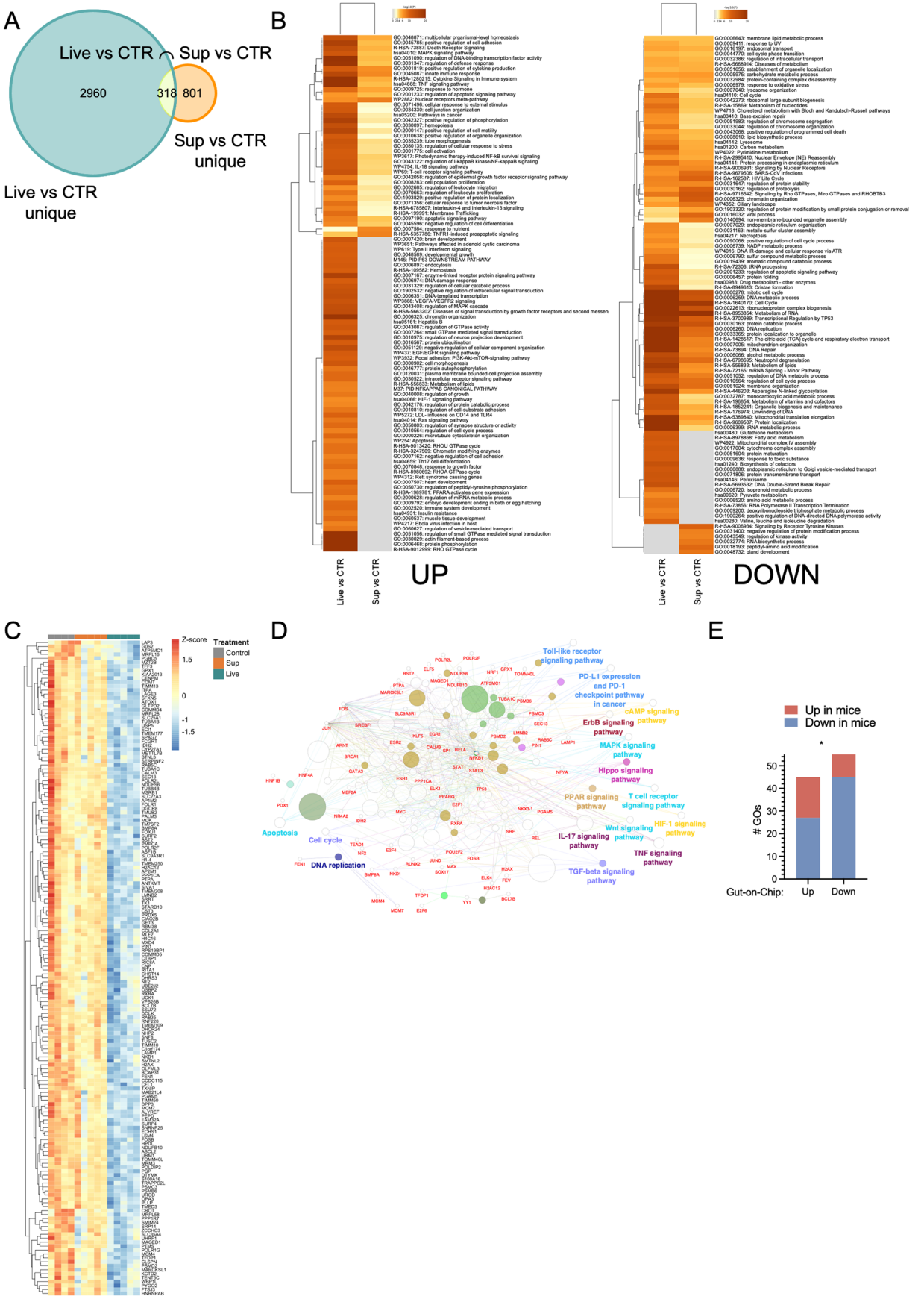

Extended Data Fig. 3 | See next page for caption.

https://doi.org/10.1038/s41551-024-01318-z

Extended Data Fig. 3 | Response to live bacteria and bacterial supernatants. **A)** Venn diagram summarizing the significant DEGs in faecal and abiotic supernatants response to control. Number of total, unique and common DEGs. **B)** Heat maps of biological terms enriched by up and down regulated DEGs in faecal and abiotic supernatants response to control. **C)** Heat maps of DEGs (163) with similar patterns of expression in live and control from the common DEGs of faecal and abiotic supernatants (318). **D)** Up-stream and enrichment analysis of DEGs (163) using KEGG database. **E)**. Biological terms enriched in vivo mouse model and gut on chip model.

https://doi.org/10.1038/s41551-024-01318-z

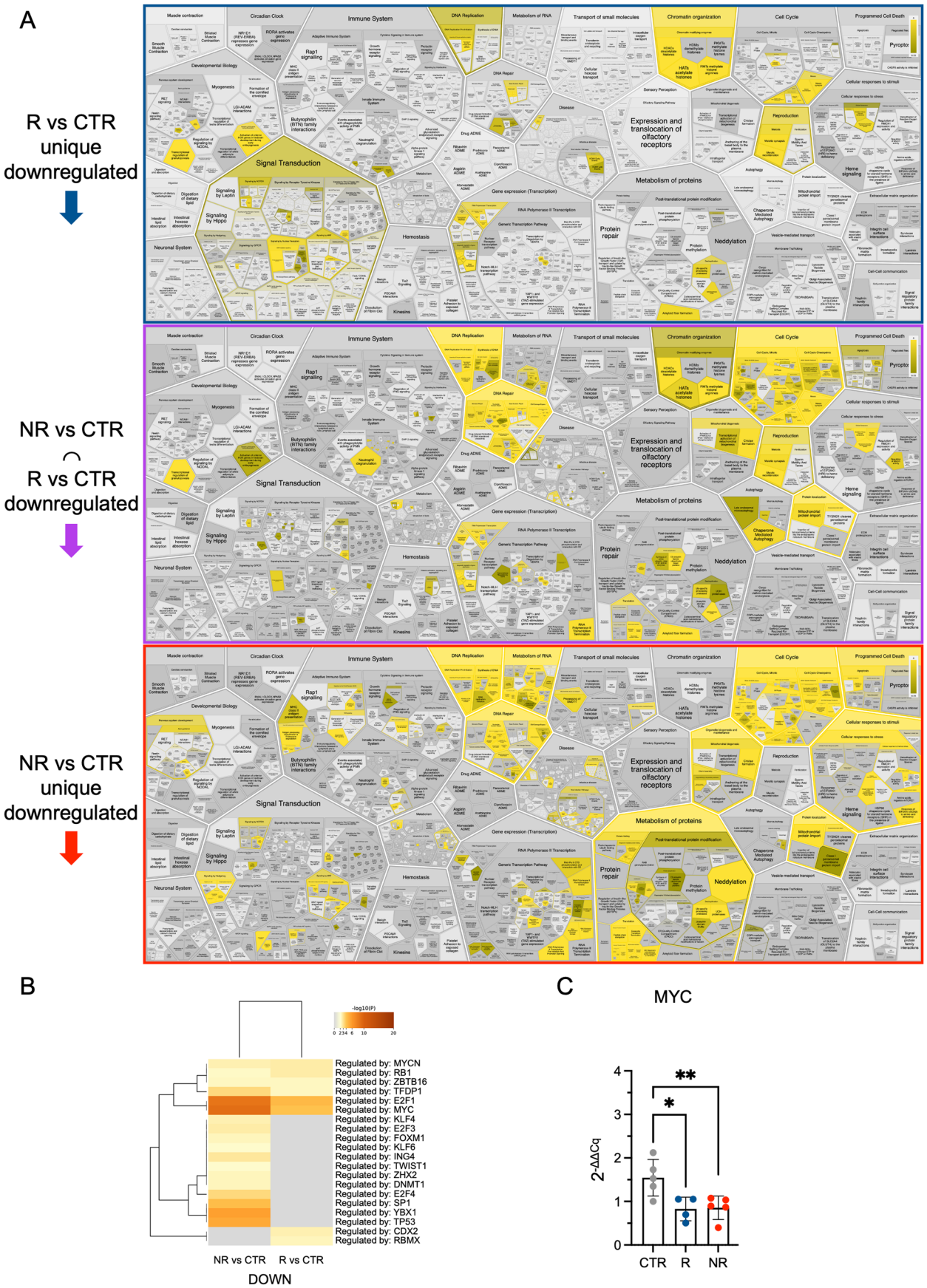

Extended Data Fig. 4 | See next page for caption.

https://doi.org/10.1038/s41551-024-01318-z

Extended Data Fig. 4 | Transcriptomic characterization of intestinal cells treated with microbiota from patients with melanoma. A) Reactome pathway analysis of NR vs CTR exclusive downregulated differentially expressed genes (DEGs), R vs CTR exclusive downregulated DEGs and common downregulated DEGs. **B)** Summary of enrichment analysis (coloured by p-values) of downregulated DEGs in TRRUST. All genes in the genome have been used as the enrichment background. Terms with a p-value < 0.01, a minimum count of 3, and an enrichment factor > 1.5 are collected and grouped into clusters based on their membership similarities. One term per cluster is shown in the figure. **C)** MYC expression (qPCR analysis) in untreated epithelial cells or epithelial cells treated with complete faecal material from faecal material of R and NR patients. Bars represent mean ± SD, two-tailed Welch's test, $p = 0.018$ for CTR vs R, $p = 0.0090$ for CTR vs NR.

https://doi.org/10.1038/s41551-024-01318-z

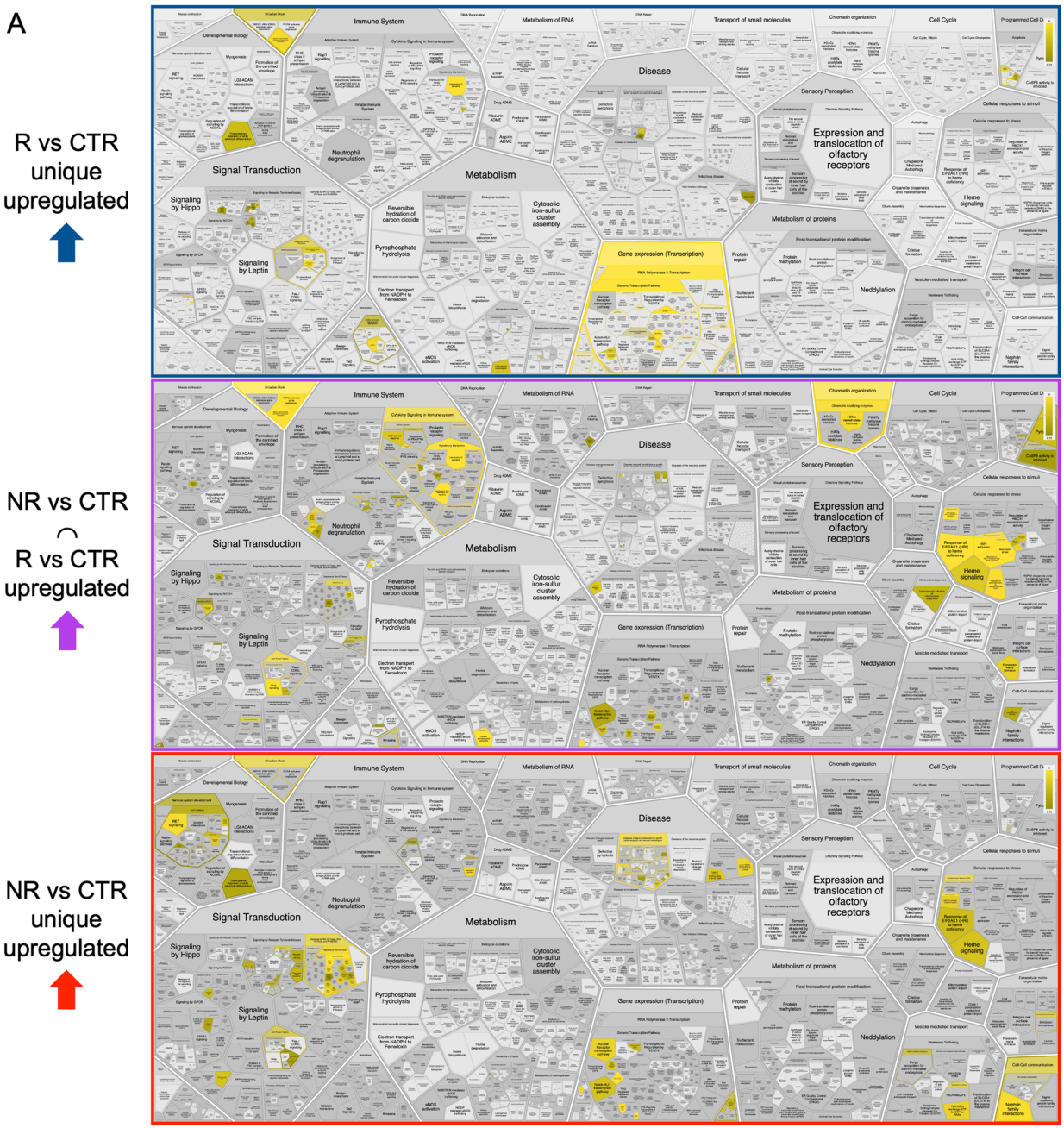

Extended Data Fig. 5 | See next page for caption.

https://doi.org/10.1038/s41551-024-01318-z

Extended Data Fig. 5 | Transcriptomic characterization of intestinal cells treated with microbiota from patients with melanoma. A) Reactome pathway analysis of NR vs CTR exclusive upregulated differentially expressed genes (DEGs), R vs CTR exclusive upregulated DEGs and common upregulated DEGs. **B)** Summary of enrichment analysis (coloured by p-values) of upregulated DEGs in TRRUST. All genes in the genome have been used as the enrichment background. Terms with a p-value < 0.01, a minimum count of 3, and an enrichment factor > 1.5 are collected and grouped into clusters based on their membership similarities. One term per cluster is shown in the figure. **C)** NFKB1 expression (qPCR analysis) in untreated epithelial cells or epithelial cells treated with complete faecal material from faecal material of patients with melanoma R and NR. Bars represent mean ± SD, two-tailed unpaired t test, $p = 0.0255$ for CTR vs NR.

https://doi.org/10.1038/s41551-024-01318-z

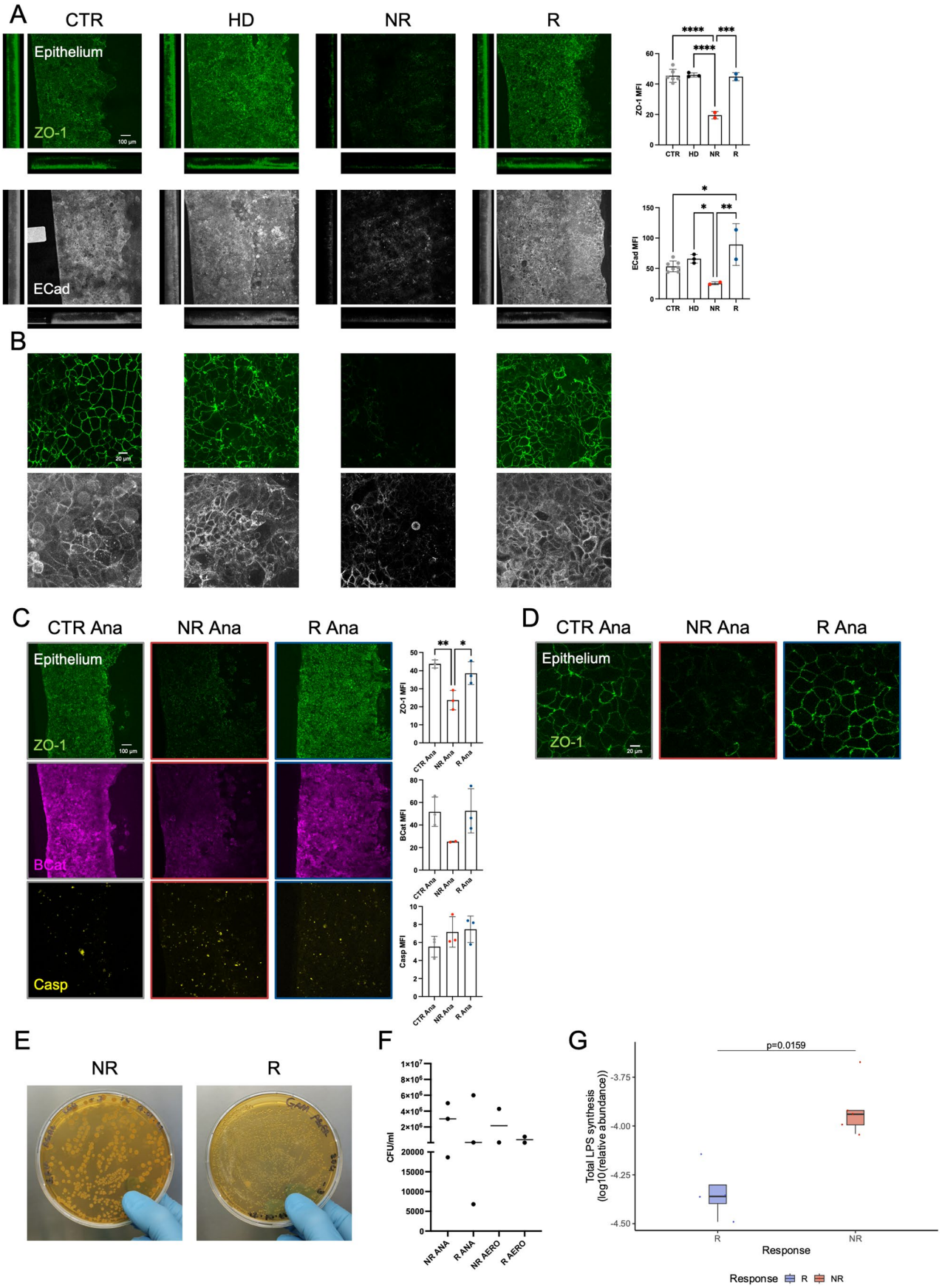

Extended Data Fig. 6 | See next page for caption.

https://doi.org/10.1038/s41551-024-01318-z

Extended Data Fig. 6 | Differences between responsive and non-responsive patients hold in comparison with faecal material from healthy donors and in anaerobic conditions. A-B) Representative fluorescence microscopy images – at lower (A) and higher (B) magnification - and mean fluorescence intensity (MFI) quantification of ZO-1 (green, n_{CTR}= 6, n_{NR}= 2, n_R= 2, n_{HD}= 3, p = 0.000034 for CTR vs NR, p = 0.000073 for HD vs NR, p = 0.0002 for NR vs R) and E-cadherin (ECad, white, n_{CTR}= 7, n_{NR}= 2 n_R= 2, n_{HD}= 3, p = 0.0304 for CTR vs NR, p = 0.0327 for HD vs NR, p = 0.0034 for NR vs R) on untreated Gut-on-Chip (CTR) or after 24h treatment with faeces (10 mg/ml) from healthy donors (HD) or patients with melanoma R or NR to immunotherapy. Scale bar 100 µm and 20 µm. Bars represent mean ± SD, ordinary one-way ANOVA. **C-D)** Representative fluorescence microscopy images – at lower (C) and higher (D) magnification - and mean fluorescence intensity (MFI) quantification of ZO-1 (green, n_{CTR}= 3, n_{NR}= 3, n_R= 3, p = 0.0059 for CTR ANA vs NR ANA, p = 0.0233 for NR ANA vs R ANA), β-catenin (Bcat, magenta, n_{CTR}= 3, n_{NR}= 2, n_R= 3) and caspase-3 (Casp, yellow, n_{CTR}= 3, n_{NR}= 3, n_R= 3) on untreated Gut-on-Chip (CTR) or after 6h treatment with faeces (10 mg/ml) from patients with melanoma R or NR to immunotherapy in anaerobic conditions. Scale bar 100 µm and 20 µm. Bars represent mean ± SD, ordinary one-way ANOVA (D upper panel). **E)** Image of faecal material from responder or non-responder patients cultured on agar plates. **F)** Colony forming unit (CFU) count in both anaerobic (ANA) and aerobic (AERO) conditions. The bacterial load from R and NR samples was comparable, however, CFUs presented different characteristics highlighting differences in the microbiota composition of the samples. **G)** Total LPS synthesis. The aggregated relative abundances (in a log10 base) of UniRef90 genes involved in lipopolysaccharide (LPS) synthesis within the faecal samples of patients (n_{NR}= 5, n_R= 4, p = 0.016, two-tailed Wilcoxon rank-sum test).

https://doi.org/10.1038/s41551-024-01318-z

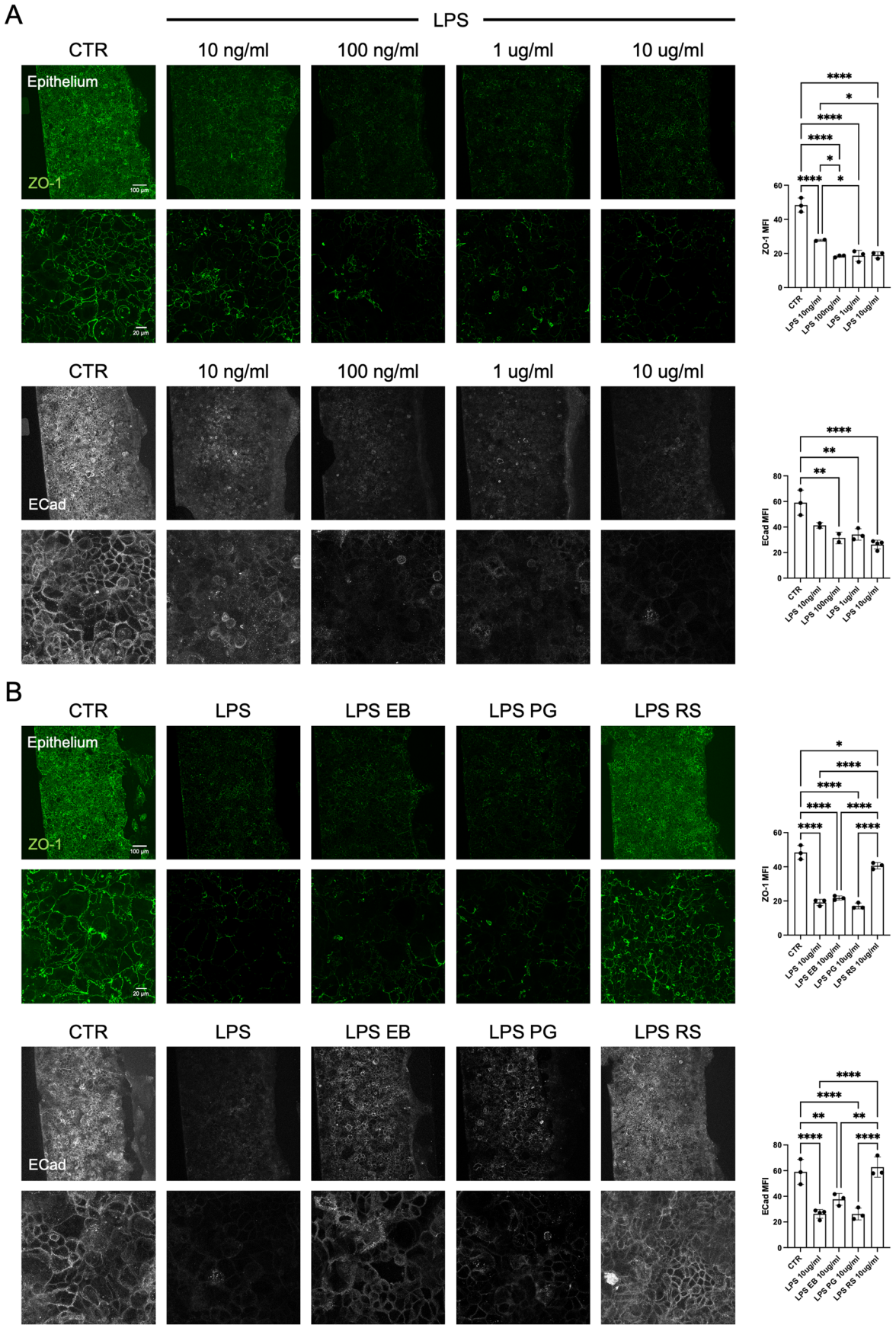

Extended Data Fig. 7 | See next page for caption.

https://doi.org/10.1038/s41551-024-01318-z

Extended Data Fig. 7 | Lipopolysaccharides (LPS) treatment on the gut-on-a-chip device. A) Representative fluorescence microscopy images and mean fluorescence intensity (MFI) quantification of ZO-1 (green, n_{CTR}= 3, nLPS10ng/ml= 2, $n_{LPS100ng/ml}$ = 3, $n_{LPS1\mu g/ml}$ = 3, $n_{LPS10\mu g/ml}$ = 3, $p < 0.0001$ for CTR vs LPS 10ng/ml, CTR vs LPS 100ng/ml, CTR vs LPS 1µg/ml, CTR vs LPS 10µg/ml, $p = 0.0132$ for LPS 10ng/ml vs LPS 100ng/ml, $p = 0.0166$ for LPS 10ng/ml vs LPS 1µg/ml, $p = 0.0251$ for LPS 10ng/ml vs LPS 10µg/ml) and E-cadherin (ECad, white, n_{CTR}= 3, $n_{LPS10ng/ml}$= 2, $n_{LPS100ng/ml}$ = 2, $n_{LPS1\mu g/ml}$ = 3, $n_{LPS10\mu g/ml}$ = 3, $p = 0.0015$ for CTR vs LPS 100ng/ml, $p = 0.0014$ for CTR vs LPS 1µg/ml, $p < 0.0001$ for CTR vs LPS 10µg/ml) on untreated Gut-on-Chip (CTR) or after 24h treatment with different concentration of LPS from *E.coli* O111:B4 (Merck). Scale bar 100 µm and 20 µm. Bars represent mean ± SD, ordinary one-way ANOVA. **B)** Representative fluorescence microscopy images and mean fluorescence intensity (MFI) quantification of ZO-1 (green, n_{CTR}= 3, n_{LPS}= 3, $n_{LPS\text{-}EB}$= 3, $n_{LPS\text{-}PG}$= 3, $n_{LPS\text{-}RS}$= 3, $p < 0.0001$ for CTR vs LPS, CTR vs LPS-EB, CTR vs LPS-PG, LPS vs LPS-RS, LPS-EB vs LPS-RS and LPS-PG vs LPS-RS, $p = 0.0236$ for CTR vs LPS-RS) and E-cadherin (ECad, white, n_{CTR}= 3, n_{LPS}= 4, $n_{LPS\text{-}EB}$= 3, $n_{LPS\text{-}PG}$= 3, $n_{LPS\text{-}RS}$= 3, $p < 0.0001$ for CTR vs LPS, CTR vs LPS-PG, LPS vs LPS-RS and LPS-PG vs LPS-R, $p = 0.0061$ for CTR vs LPS-EB, $p = 0.0012$ for LPS-EB vs LPS-RS) on untreated Gut-on-Chip (CTR) or after 24h treatment with LPS from *E.coli* O111:B4 (L2630 Merck), *E.coli* O111:B4 (EB, tlrl-3pelps InvivoGen), *Porphyromonas gingivalis* (PG, tlrl-ppglps InvivoGen) and *Rhodobacter sphaeroides* (RS, tlrl-prslps InvivoGen). Scale bar 100 µm and 20 µm. Bars represent mean ± SD, ordinary one-way ANOVA.

https://doi.org/10.1038/s41551-024-01318-z

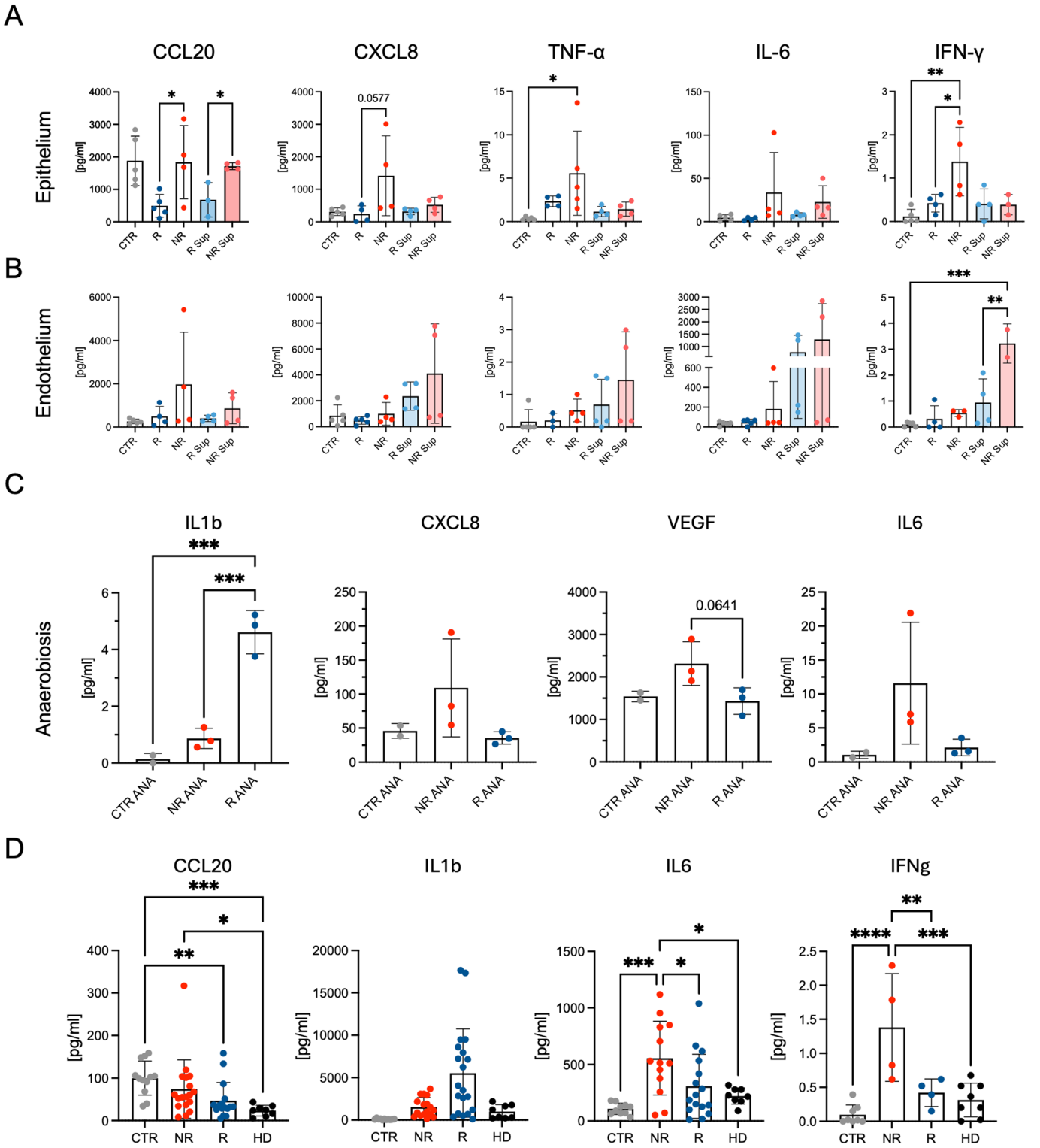

Extended Data Fig. 8 | Inflammatory response of the gut-on-a-chip in different experimental conditions. A-D) Multiplex ELISA (Luminex) quantification in the epithelial (A) and endothelial (B) channels of the indicated cytokines in anaerobic conditions (C) or in comparison with healthy donors (D). Bars represent mean ± SD, two-tailed unpaired t test (A left p = 0.0379 for R vs NR and p = 0.011 for R Sup vs NR Sup), ordinary one-way ANOVA (A center p = 0.0227, A right p = 0.003, B p = 0.0001 for CTR vs NR Sup and p = 0.0026 for R Sup vs NR Sup, C p = 0.0006 for CTR vs R and p = 0.0009 for R vs NR, D center p = 0.0004 for CTR vs NR, p = 0.036 for R vs NR and p = 0.0187 for NR vs HD, D right p = 0.000062 for CTR vs NR, p = 0.00467 for R vs NR and p = 0.000478 for NR vs HD), Kruskal-Wallis test (D left p = 0.0069 for CTR vs R, p = 0.0004 for CTR vs HD and p = 0.0318 for NR vs HD).

nature portfolio

Corresponding author(s): Luigi Nezi

Last updated by author(s): Oct 8, 2024

Reporting Summary

Nature Portfolio wishes to improve the reproducibility of the work that we publish. This form provides structure for consistency and transparency in reporting. For further information on Nature Portfolio policies, see our Editorial Policies and the Editorial Policy Checklist.

Statistics

For all statistical analyses, confirm that the following items are present in the figure legend, table legend, main text, or Methods section.

n/a	Confirmed	
☐	☒	The exact sample size (*n*) for each experimental group/condition, given as a discrete number and unit of measurement
☐	☒	A statement on whether measurements were taken from distinct samples or whether the same sample was measured repeatedly
☐	☒	The statistical test(s) used AND whether they are one- or two-sided *Only common tests should be described solely by name; describe more complex techniques in the Methods section.*
☐	☒	A description of all covariates tested
☐	☒	A description of any assumptions or corrections, such as tests of normality and adjustment for multiple comparisons
☐	☒	A full description of the statistical parameters including central tendency (e.g. means) or other basic estimates (e.g. regression coefficient) AND variation (e.g. standard deviation) or associated estimates of uncertainty (e.g. confidence intervals)
☐	☒	For null hypothesis testing, the test statistic (e.g. *F*, *t*, *r*) with confidence intervals, effect sizes, degrees of freedom and *P* value noted *Give P values as exact values whenever suitable.*
☒	☐	For Bayesian analysis, information on the choice of priors and Markov chain Monte Carlo settings
☒	☐	For hierarchical and complex designs, identification of the appropriate level for tests and full reporting of outcomes
☒	☐	Estimates of effect sizes (e.g. Cohen's *d*, Pearson's *r*), indicating how they were calculated

Our web collection on statistics for biologists contains articles on many of the points above.

Software and code

Policy information about availability of computer code

Data collection	- Sequencing data were collected using Illumina sequencing platforms (NovaSeq 6000 System) - Multiplex ELISA data were collected using a Luminex 200. - Confocal laser-scanning microscopy was performed using an Inverted Leica SP8AOBS (Leica).
Data analysis	- Images were analyzed and quantified using Fiji (ImageJ, Version 2.0.0-rc-59/1.51n). - Whole genome shotgun sequencing data were processed using the pipeline from https://github.com/SegataLab/preprocessing, taxonomy and functional profiles were produced using tools from the biobakery3 pipeline, and data were analyzed in R using functions from gtools for fold-change computations, rstatix for taxonomy rankings. - Raw paired-end reads were subjected to quality check using the FastQC v 0.11.9 tool, trimmed using Trimmomatic v 0.392, aligned using STAR aligner v 2.7.10a to the reference genome GRCh38, quantified using the feature counts v 2.0.2. - Differential expression analysis was performed using the edgeR, the PCA was calculated using the R base prcomp and the plots to identify the batch effect was generated using the ggplot2 v 3.4.16. To obtain the DEGs the log-cpm values were subjected to limma-voom pipeline. Functional profiling was carried using Metascape v 3.5.27. To upstream analysis and visualization was done on Metascape and NetworkAnalyst v3. The list of DEGs were mapped to the KEGG database using Cytoscape's ClueGo plugin. - All data were analyzed using R version 4.1.1. and PRISM version 9.2 - Code to reproduce plots of the manuscript is available at https://github.com/Punit201016/Gut_on_Chip. The raw sequence data are available with accession number E-MTAB-13312 on the Annotare 2.0, ArrayExpress database (https://www.ebi.ac.uk/biostudies/arrayexpress). The remaining data are available within the Article or Supplementary Information file.

For manuscripts utilizing custom algorithms or software that are central to the research but not yet described in published literature, software must be made available to editors and reviewers. We strongly encourage code deposition in a community repository (e.g. GitHub). See the Nature Portfolio guidelines for submitting code & software for further information.

Data

Policy information about availability of data

All manuscripts must include a data availability statement. This statement should provide the following information, where applicable:

- Accession codes, unique identifiers, or web links for publicly available datasets
- A description of any restrictions on data availability
- For clinical datasets or third party data, please ensure that the statement adheres to our policy

The transcriptomic data generated in this study is deposited on the zenodo and can be accessed using the link https://zenodo.org/records/13889913. The raw sequence data are available with accession number E-MTAB-13312 on the Annotare 2.0, ArrayExpress database (https://www.ebi.ac.uk/biostudies/arrayexpress).

Research involving human participants, their data, or biological material

Policy information about studies with human participants or human data. See also policy information about sex, gender (identity/presentation), and sexual orientation and race, ethnicity and racism.

Reporting on sex and gender	Sex was self-reported by subjects enrolled. Gender informations were not collected.
Reporting on race, ethnicity, or other socially relevant groupings	Patients enrolled in this study were not grouped based on race, ethnicity or other socially relevant characteristics.
Population characteristics	Patients with stage IIIB-C melanoma (n= 10) undergoing aniti-PD-1 therapy (either Nivolumab or Pembrolizumab). No pther covariants were considered.
Recruitment	Patients were enrolled at Istituto Europeo di Oncologia (IEO, Milan) between 2018 and 2020 after signing an informed consent form approved by the local Ethical Committee (study registered as R845/18-IEO 889). Samples from all available participants were tested with no bias-selection. No compensation was paid to patients for participating in the study. Fecal material from healthy donors were obtained at European Institute of Oncology IRCCS with a protocols were approved by IEO Ethical Committees (registered as IEO1271).
Ethics oversight	The protocol has been approved by th IEO Ethical Committee (registered as IEO1271). Donors provided written informed consent to biological sample collection, analysis and data publication according to Declaration of Helsinki. Samples were numerically coded to protect donor's rights to confidentiality and privacy.

Note that full information on the approval of the study protocol must also be provided in the manuscript.

Field-specific reporting

Please select the one below that is the best fit for your research. If you are not sure, read the appropriate sections before making your selection.

☒ Life sciences ☐ Behavioural & social sciences ☐ Ecological, evolutionary & environmental sciences

For a reference copy of the document with all sections, see nature.com/documents/nr-reporting-summary-flat.pdf

Life sciences study design

All studies must disclose on these points even when the disclosure is negative.

Sample size	The number of patients included in the analysis aimed to balance the number of samples in each response group and to obtain statistically significant results in the performed experiments.
Data exclusions	No data were excluded.
Replication	The experimental findings were reliably reproduced (n>2). Number of biological and experimental replicates are stated in the manuscript.
Randomization	No randomization was applied since these patients were all eligible for immunotherapy with the Italian Public Health System.
Blinding	Whenever possible/feasible, samples informations were hidden to the investigator during experimental run and analysis. The samples were identified into groups at the stage of entering the data into the statistical analysis.

Reporting for specific materials, systems and methods

We require information from authors about some types of materials, experimental systems and methods used in many studies. Here, indicate whether each material, system or method listed is relevant to your study. If you are not sure if a list item applies to your research, read the appropriate section before selecting a response.

Materials & experimental systems

n/a	Involved in the study
☐	☒ Antibodies
☐	☒ Eukaryotic cell lines
☒	☐ Palaeontology and archaeology
☒	☐ Animals and other organisms
☒	☐ Clinical data
☒	☐ Dual use research of concern
☒	☐ Plants

Methods

n/a	Involved in the study
☒	☐ ChIP-seq
☒	☐ Flow cytometry
☒	☐ MRI-based neuroimaging

Antibodies

Antibodies used

All antibodies used in our study are commercially available and validated. Antibodies for Luminex assay were provided as pre-mix by vendor (R&D). Zonula occludens-1 (ZO-1, 1:100, Invitrogen, #Cat339188), E-cadherin (1:200, Abcam, #Catab1416), □-catenin (1:200, BD Bioscience, #Catab8480), Villin (1:100, Santa Cruz, #Catsc-58897), Ki67 (1:500, Abcam, #Catab15580), Cleaved Caspase-3 (1:400, Cell Signaling, #Cat9661S), MUC2 (1:100, ThermoFisher, #CatMA5-12345), MUC5AC (1:100, Invitrogen,#CatMA5-12178), VE-cadherin (1:400, Abcam, #Catab33168) and ICAM-1 (1:250, BD Bioscience, #CatVE297946).

Validation

All antibodies used in our study are commercially available and validated and informations available at their respective manufacturer's websites.

Eukaryotic cell lines

Policy information about cell lines and Sex and Gender in Research

Cell line source(s)

Caco-2 cells were obtained from ATCC.
HT-29 MTX cells were generated from commercial HT-29 (ATCC) and donated as a gentle gift generated by Dr. Monteleone (Univ. of Rome Tor Vergata).
Human Microvascular Endothelial Cells (HMEC-1) were obtained from Center for Disease Control and Prevention (CDC, Atlanta, GA).
Human iPSCs were obtained from The Jackson Laboratory (www.jax.org, KOLF2.1J).

Authentication

None of the cell lines used where authenticated

Mycoplasma contamination

All cell lines tested negative for Mycoplasma test.

Commonly misidentified lines
(See ICLAC register)

N/A

Plants

Seed stocks

Report on the source of all seed stocks or other plant material used. If applicable, state the seed stock centre and catalogue number. If plant specimens were collected from the field, describe the collection location, date and sampling procedures.

Novel plant genotypes

Describe the methods by which all novel plant genotypes were produced. This includes those generated by transgenic approaches, gene editing, chemical/radiation-based mutagenesis and hybridization. For transgenic lines, describe the transformation method, the number of independent lines analyzed and the generation upon which experiments were performed. For gene-edited lines, describe the editor used, the endogenous sequence targeted for editing, the targeting guide RNA sequence (if applicable) and how the editor was applied.

Authentication

Describe any authentication procedures for each seed stock used or novel genotype generated. Describe any experiments used to assess the effect of a mutation and, where applicable, how potential secondary effects (e.g. second site T-DNA insertions, mosiacism, off-target gene editing) were examined.